Molecular Catalysis 492 (2020) 110964

Contents lists available at ScienceDirect

Molecular Catalysis

journal homepage: www.elsevier.com/locate/mcat

Spectroscopic and kinetic insights into the methane reforming over Ce-pyrochlores

Disha Jain*, Shreya Saha

Department of Chemical Engineering, Indian Institute of Science, Bangalore 560012, India

ARTICLE INFO

Keywords:
DRIFTS
Methane reforming
Kinetics
Pyrochlores
Surface chemistry

ABSTRACT

High thermal stability and oxygen conductivity of pyrochlores makes them a potential catalyst for the dry reforming of methane (DRM). In this study, noble metal (Pt, Ru) substituted $Ce_2Zr_2O_7$ and $Ce_2Ti_2O_7$ pyrochlores have been synthesized by modified Pechini method. The effect of variation of dopant concentration and position was examined to achieve strong metal-support interaction. $Ce_2Zr_{1.96}Pt_{0.04}O_{7-\delta}$ exhibited the best catalytic activity towards DRM and hence, been studied for partial oxidation (POM) and autothermal reforming of methane (ATR). Syngas ratio (H_2/CO) was tuned by varying the O_2 concentration in the feed. Insights obtained from both *ex-situ* and *in situ* characterization were exploited to discern the reaction mechanism. The surface intermediates were examined by DRIFTS on $Ce_2Zr_{1.96}Pt_{0.04}O_{7-\delta}$ for DRM, POM and ATR. Besides adsorbed CH_4 and CO on Pt, the presence of carbonate and formate species were also identified. Thus, a dual-site mechanism via carbonate and formate formation was proposed for DRM over $Ce_2Zr_{1.96}Pt_{0.04}O_{7-\delta}$.

1. Introduction

CH_4 and CO_2 are the major greenhouse gases, with CH_4 having higher potency towards global warming than CO_2 [1]. Among the various routes exploited for transforming methane into value-added products, syngas production is the most feasible process [2]. Moreover, many natural gas reserves and biogas obtained from anaerobic degradation of organic matter contain considerable amount of CO_2 [3,4]. Carbon dioxide or dry reforming of methane (DRM) can utilize the natural gas with large CO_2 content, thereby avoiding the costly gas separation processes [4]. The syngas ratio (H_2/CO) attained via DRM is nearly unity, which is suitable for Fischer-Tropsch synthesis of long chain hydrocarbons and oxygenated chemicals [3,5,6]. The major problems encountered in reforming reaction are methane activation, coke deposition due to methane decomposition and Boudouard reaction, thermal deactivation of support and side reactions like reverse water-gas shift reaction [7,8].

Numerous permutations of active metal and support have been investigated in the literature to enhance metal-support interaction [7,9]. For instance, to reduce the deactivation due to sintering, the dispersion of active metal over the support can be increased that leads to enhanced metal-support interaction. The basic support suppresses coke deposition by improving the adsorption of CO_2, which is mildly acidic [10,11]. Nonetheless, the supported catalysts suffer from the problem of coke deposition on active metal. These difficulties can be overcome by the incorporation of active metal into the lattice of oxide. Substitution of active metal in the oxide lattice alters the reaction mechanism by influencing the activation of the reactant species and by modifying the stability of the reaction intermediates [12]. Metal substitution eliminates the problem of metal sintering and also reduces carbon deposition by tailoring the reducibility of the support.

Activation of CH_4 is a critical step in the dry reforming of methane due to high dissociation energy of C—H bond (439 kJ/mol) [8]. In supported metal catalyst, C—H bond splits by the addition of Pt atom (or any active metal) into C—H bond with back donation of electron from Pt to antibonding state of C—H, resulting in (H_3C–Pt—H) transition state [13]. However, the mechanism of activation of C—H is different for Pt-substituted oxide due to the electronic modifications induced by metal doping. New energy levels are created due to the hybridization of *d*-states of dopant and parent atom. The delocalized d-states of transition metal hybridize with O 2p creating energy levels that are responsible for the formation of various impurities in the oxide [14]. Additionally, for aliovalent dopant, oxide vacancies are formed that results in creation of defect energy levels between conduction band and valence band [15]. Schwarz et al. suggests that the high charge density at the terminal oxygen plays a key role in C—H bond cleavage by the transfer of hydrogen atom from CH_4 to oxide [16]. Further, as an effect of doping on the hydrogen atom transfer, there is an increase in

* Corresponding author.
E-mail address: disha@iisc.ac.in (D. Jain).

https://doi.org/10.1016/j.mcat.2020.110964
Received 3 December 2019; Received in revised form 12 April 2020; Accepted 13 April 2020

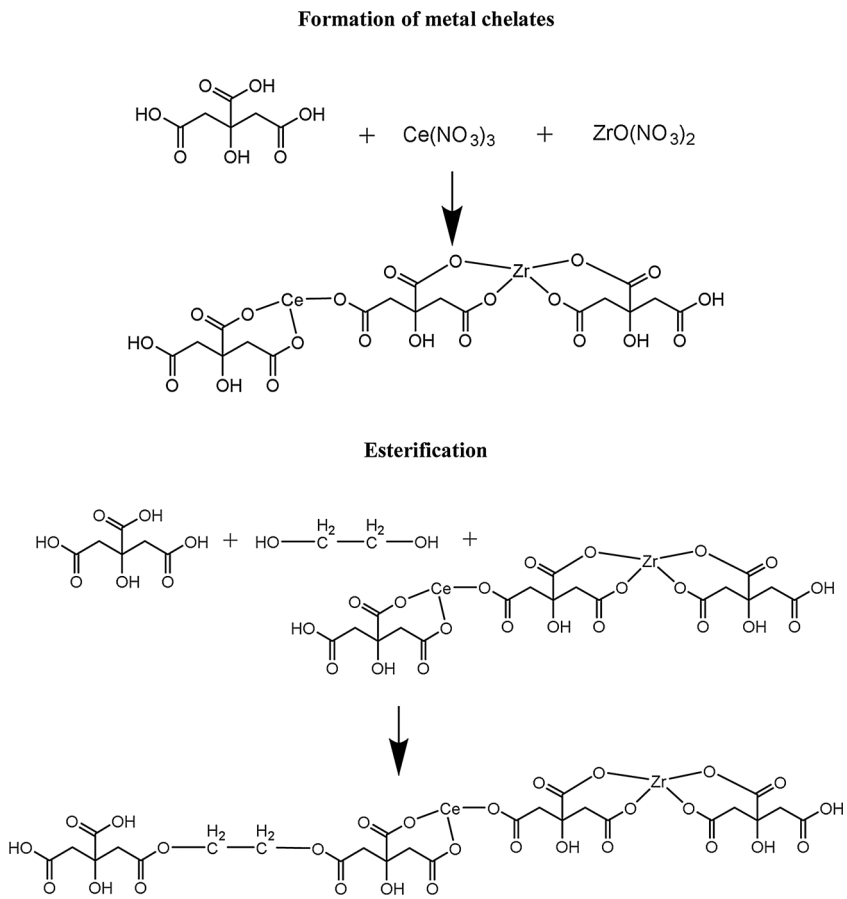

Scheme 1. Reaction steps involved in modified Pechini method.

charge density on the bridging oxygen of MgO after doping with Ga_2O_3 [17]. Therefore, the integration of metal in the oxide lattice can result in formation of new active sites besides forming stable catalyst towards methane reforming.

Pyrochlores are ternary oxides of type $A_2B_2O_7$, which are stable at high temperature and have high oxygen conductivity. For a stable pyrochlore structure, the radius ratio (r_A/r_B) should lie between 1.46 and 1.78. These oxides have vacancies at A and O sites that enhances the migration of oxygen ion in the lattice [8]. These properties make pyrochlore a potential catalyst for dry reforming of methane. However, pyrochlore supports have low surface area that might limit the dispersion of active metal leading to reduction in the catalytic activity and coke deposition [18]. Consequently, the substitution of active metal in the pyrochlore lattice will yield a stable and active catalyst. Pakhare et al. have studied the kinetics of the Rh-substitution on $La_2Zr_2O_7$ pyrochlore towards dry reforming of methane and proposed a dual-site mechanism [19] La-pyrochlores are extensively studied in literature for dry reforming of methane with noble metal substitution at B site [20,21]. However, there are limited studies on Ce-pyrochlores for methane reforming. CeO_2 has been studied for DRM due to its oxygen storage capacity, which is a beneficial attribute in mitigating coke deposition during methane reforming. Owing to its low thermal stability, the mixed oxides of $Ce_{1-x}Zr_xO_2$, $Ce_{1-x}Pr_xO_2$ supported Ni catalysts were investigated, however, the problem of formation of carbon filaments and NiO still remains [22–25]. Mizuki et al. reported $Ni/Ce_2Zr_2O_x$ for steam reforming of methane, but, the kinetics over $Ce_2Zr_2O_x$ pyrochlores remains unexplored [26]. The change in oxygen concentration of $Ce_2Zr_2O_{7+x}$ compounds by detailed XRD analysis has been discussed in several studies [27–29] The comprehensive structural studies reported by Achary et al. highlights the excellent oxygen storage capacity of $Ce_2Zr_2O_{7+x}$ [27]. The facile conversion between Ce^{3+} and Ce^{4+} can easily occur in these structures, while retaining the cubic symmetry [30].

In this work, we have studied dry reforming of methane over noble metal (NM: Pt, Ru) substituted $Ce_2Zr_2O_7$ and $Ce_2Ti_2O_7$ pyrochlores synthesized by modified Pechini method. The catalytic activity of $Ce_2Zr_{1.96}Pt_{0.04}O_{7-\delta}$ towards partial oxidation of methane and autothermal methane reforming has been investigated. The synthesized samples were characterized by X-ray diffraction (XRD), X-ray photoelectron spectroscopy (XPS) and transmission electron microscopy (TEM). Diffuse reflectance infrared Fourier transform spectroscopy (DRIFTS) was performed to determine the abundant surface intermediates formed during the reaction. Subsequently, a comprehensive reaction mechanism was proposed over $Ce_2Zr_{1.96}Pt_{0.04}O_{7-\delta}$ and a detailed kinetic model was derived based on the insights obtained from the above studies.

2. Experimental

2.1. Materials

Two series of cerium based pyrochlores were synthesized viz. $Ce_2Ti_2O_7$ and $Ce_2Zr_2O_7$. The metal precursors used for the synthesis of these pyrochlores were cerium (III) nitrate hexahydrate ($Ce(NO_3)_3.6H_2O$, S.D. fine Chemicals, India), zirconium (IV) oxynitrate ($ZrO(NO_3)_2$, Sigma Aldrich, U.S.A.) and titanium isopropoxide ($Ti(OCH(CH_3)_2)_4$, Sigma Aldrich, U.S.A.). Ruthenium chloride ($RuCl_3$, TCI chemicals, Japan) and tetraammine platinum nitrate ($Pt(NH_3)_4(NO_3)_2$, Alfa Aesar, U.S.A.) were used as dopant precursors, while, citric acid (Merck, India) and ethylene glycol (S.D. fine Chemicals, India) were used as complexing agent and polymerizing agent, respectively.

2.2. Methods

2.2.1. Synthesis of Ce-pyrochlores

Noble metal (NM- Pt, Ru) doped Ce-pyrochlores *i.e.* $Ce_2Zr_{1.96}Pt_{0.04}O_{7-\delta}$, $Ce_2Zr_{1.96}Ru_{0.04}O_{7-\delta}$, and $Ce_2Ti_{1.96}Pt_{0.04}O_{7-\delta}$ were prepared by modified Pechini method [21]. For the synthesis of $Ce_2Zr_{1.96}Pt_{0.04}O_{7-\delta}$, 2 mol of $Ce(NO_3)_3.6H_2O$, 1.96 mol of $ZrO(NO_3)_2$ and 0.04 mol of $Pt(NH_3)_4(NO_3)_2$ were dissolved in deionized water. An aqueous solution of citric acid (CA) was added to the above solution, maintaining the molar ratio of citric acid and total metal ion as 1.2:1. The temperature of the solution mixture was raised to 70 °C, with continuous stirring to ensure complete chelation of metal ions with citric acid. Now, ethylene glycol (EG) was added to the solution with EG:CA as 1:1. The solution was maintained at 70 °C until a viscous transparent gel was obtained. The temperature of the solution was then increased to enhance the degree of esterification reaction by removing water. During this stage, violent bubbling and frothing of gel was observed with the emission of brown fumes of NO_x formed as a result of the decomposition of metal nitrates. An amorphous solid product thus obtained was calcined at 750 °C for 3 h to achieve a crystalline pyrochlore oxide. Ethanol was used as solvent for synthesizing $Ce_2Ti_{1.96}Pt_{0.04}O_{7-\delta}$, as titanium isopropoxide decomposes in water. The various reaction steps involved in the synthesis of $Ce_2Zr_2O_7$ pyrochlores are depicted in Scheme 1. 4 at% Pt impregnated over $Ce_2Zr_2O_7$ was synthesized by impregnation method, where the slurry of synthesized $Ce_2Zr_2O_7$ was prepared in deionized water and stoichiometric quantity of $Pt(NH_3)_4(NO_3)_2$. Pt ions were reduced with the help of hydrazine hydrate over $Ce_2Zr_2O_7$. The aging of this mixture was done for an hour and thereafter, the mixture was washed with ethanol several times to obtain pH = 7. The sample was dried and then reduced in H_2 flow at 700 °C for 2 h and was represented as 4% Pt/ $Ce_2Zr_2O_7$.

2.3. Characterization

The structural characterization of the synthesized compounds was done using XRD, XPS and TEM. XRD pattern was acquired at 25 °C with Rigaku X-ray diffractometer employed with Cu-Kα radiation (λ = 1.5418 Å) and Ni filter. XRD pattern was collected in the 2θ range from 10° to 80° with steps of 0.02°. XRD was performed to do phase analysis in the synthesized samples. X-ray photoelectron spectra (XPS) were recorded on AXIS ULTRA instrument with Al-Kα (1486.6 eV) as source and pass energy of 20 eV. The samples were etched with Ar^+ for 30 s and 4 keV to remove the adsorbed oxygen and hydroxyl species. XPS was performed to determine the elemental states of the samples before and after the reaction. The charging correction for all the samples has been done using adventitious carbon (*i.e.* C—C) with binding energy of 284.8 eV. The particle size and crystalline phases of the material were determined by TEM on Technai F-30, operating at 200 kV. The solution of the material dispersed in ethanol was drop casted on the carbon coated Cu grids (400 mesh size). The surface area measurement was performed on Belsorb surface area analyzer (Smart instruments) using BET nitrogen sorption method at 77 K. The synthesized samples were regenerated at 150 °C for 3 h to remove any adsorbed water and CO_2. Coke deposition on the spent catalyst was determined by thermogravimetric analysis (TGA) by NETZSCH STA 409. A crucible containing 6–8 mg of sample was heated in a furnace from 30 to 800 °C in nitrogen atmosphere. The bulk composition of noble metals was determined by inductively plasma coupled mass spectroscopy (ICP-MS, Thermo X series). For ICP analysis, 20 mg of sample was dissolved in aqua regia and then after dissolution, aqua regia was evaporated. The digested samples were diluted with 2% HNO_3 for analysis.

2.4. H_2 temperature programmed reduction

Reduction studies by H_2 were performed to investigate the reducibility of the noble metal substituted pyrochlores. 10 mg of sample was packed inside the quartz tube (I.D. - 4 mm) and reduced in 5% H_2/Ar gas flow of 30 mL/min. H_2 uptake was measured using thermal conductivity detector (TCD) as a function of temperature, increased at constant ramp rate of 10 °C/min. The quantity of H_2 consumed was calibrated with CuO.

2.5. CO temperature programmed desorption

Temperature programmed desorption was performed in the presence of CO over $Ce_2Zr_{1.96}Pt_{0.04}O_{7-\delta}$, to determine the exposed Pt atom on the surface of the catalyst. The sample (20 mg) was filled in the quartz tube (I.D. - 4 mm) between two ceramic wool plugs. In first step, the sample was degassed in He flow at 200 °C to remove the adsorbed water and CO_2 from the surface and was then cooled to room temperature. Pulse injection of CO was done and CO was allowed to adsorb over the sample under He flow of 25 mL/min. The desorption of CO was studied by increasing the temperature from 30 to 650 °C at constant rate of 10 °C/min and quantity of CO was recorded by Thermal conductivity detector (TCD).

2.6. Catalytic activity

The catalytic studies *i.e.* dry reforming of methane (DRM), partial oxidation of methane (POM) and autothermal reforming (ATR) were conducted in the packed bed reactor. 100 mg of catalyst was packed in the quartz tube between the ceramic wool plugs in the form of granules, which are in the size range of 150 − 300 μm. The catalyst was diluted with an inert material *i.e.* silica gel so as to maintain the bed length as 1 cm. The reactor was placed inside the furnace and the thermocouple was positioned in the center of the catalyst bed. A PID controller was used for maintaining the temperature of the catalyst bed within ± 1 °C. The product gases were analyzed at various temperatures under isothermal conditions. The feed gas mixture for DRM consisted of 3% CH_4 (99 %, Chemix gases, Bangalore), 3 % CO_2 (99 %, Chemix gases, Bangalore) and rest N_2 (99 %, Noble gases, Bangalore), however, few reaction were performed at high concentration- 20 % CH_4 with CH_4:CO_2 – 1, to study coke deposition. POM reaction was performed with the reactant gas ratio *i.e.* CH_4:O_2 as 1:0.5 with 3% CH_4. ATR was performed at three different O_2 (99 %, Noble gases, Bangalore) concentrations *i.e.* CH_4:CO_2:O_2 was varied as 1:1:0.1, 1:1:0.2 and 1:1:0.5 to determine the effect of O_2 concentration on syngas ratio. The total gas flow rate was maintained at 80 mL/min for all the reaction studies. The GHSV of 38,120 h^{-1} was calculated based on the total bed volume (0.125 cm^3) and was maintained constant for all the experiments. The product gases were analyzed using gas chromatograph (Mayura Analytical Ltd., India), which was fitted with flame ionization detector (FID), TCD and methanator. FID was used for analyzing CO, CH_4 and CO_2, whereas, H_2 was detected in TCD. The methanator (positioned before FID) was equipped with Ru catalyst which was maintained at 350 °C and used for converting CO and CO_2 to CH_4, due to weak signals of CO and CO_2 in FID. A moisture trap was placed at the exit of the reactor to condense water, if formed during the reaction, as water cannot be allowed to enter the gas chromatograph.

2.7. In situ FTIR (DRIFTS) studies

In situ FTIR (DRIFTS) studies were performed on Frontier, Perkin Elmer, which was fitted with DTGS detector. The experimental set up consisted of an *in situ* DRIFTS cell with ZnSe windows (Harrick, Model # HVC-DWM-3), which is placed inside Praying Mantis (Model # HVC-DRP-4). This high temperature reaction chamber was fitted with a heating cartridge and was coupled with a chiller for maintaining temperature. A PID controller (Harrick, Model # ATC-024-4) was employed for maintaining the temperature of the cell within ± 1 °C. The catalyst (~50 mg) was filled in the DRIFTS cell and the reactant gases were passed over the catalyst. The composition of the reactant gas for DRM,

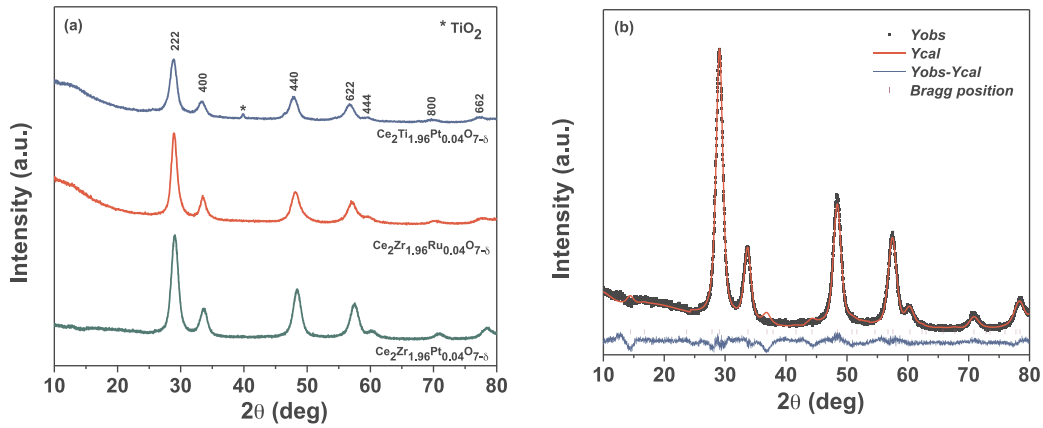

Fig. 1. (a) XRD pattern of the noble metal substituted pyrochlores; (b) Rietveld refined XRD pattern of $Ce_2Zr_{1.96}Pt_{0.04}O_{7-\delta}$.

POM and ATR reaction was 3 % CH_4, 3 % CO_2, rest N_2, 3 % CH_4, 1.5 % O_2, rest N_2 and 3 % CH_4, 3 % CO_2, 1.5 % O_2, rest N_2, respectively. The composition was maintained constant for a particular reaction studies. The spectra were acquired at four different temperatures *i.e.* 28, 350, 450 and 600 °C. The background was recorded at each temperature before starting the analysis under N_2 flow. All the spectra were recorded with 32 scans and the resolution of 4 cm^{-1}. The chamber was purged with N_2 while the temperature was increased. DRIFTS investigations were performed for $Ce_2Zr_{1.96}Pt_{0.04}O_{7-\delta}$.

3. Results and discussion

3.1. Structural characterization

3.1.1. X-ray diffraction

Fig. 1a shows the XRD pattern of all the synthesized samples. It is evident from the XRD patterns that $Ce_2Zr_{1.96}Pt_{0.04}O_{7-\delta}$ and $Ce_2Zr_{1.96}Ru_{0.04}O_{7-\delta}$ crystallized in the pyrochlore structure. However, the pyrochlore phases of $Ce_2Ti_{1.96}Pt_{0.04}O_{7-\delta}$ were accompanied by the presence of some phase of TiO_2. The shift in 2θ values of some reflections in the synthesized samples may be attributed to the doping of NM (Pt. Ru) in the oxide lattice. Owing to the presence of intrinsic oxide vacancy in $Ce_2Zr_2O_7$, it can accept oxygen atom to annihilate oxide vacancies forming $Ce_2Zr_2O_8$. Arai et al. observed the existence of $Ce_2Zr_2O_{7.5}$, which is a metastable phase, as a result of adsorption of ambient oxygen at room temperature [31]. However, due to the dominant scattering from heavy metals like Ce and Zr, the small change in stoichiometry of oxygen cannot be observed in XRD [27].

XPS (see Section 3.1.2) was employed to acquire the elemental composition of Ce. The ratio of Ce^{3+}:Ce^{4+} was obtained from the deconvolution of Ce 3d XP spectra and was found to be 0.45:0.55. This suggests the possibility of existence of synthesized samples in $Ce_2Zr_2O_{7.5}$ phase. As a result of rearrangement, *Fd-3 m* symmetry in $Ce_2Zr_2O_7$ is changed to *F-43 m* in $Ce_2Zr_2O_{7.5}$ [27,31]. Hence, the XRD pattern calculated by Sasaki et al. (from ICSD) was used to refine the experimental XRD pattern of $Ce_2Zr_{1.96}Pt_{0.04}O_{7-\delta}$ [29]. XRD pattern of $Ce_2Zr_{1.96}Pt_{0.04}O_{7-\delta}$ was refined by GSAS and EXPGUI and the fitted pattern is shown in Fig. 1b. Manual background subtraction was performed with 18 terms and pseudo-voigt function was used for fitting profile. The goodness of the fit was determined by the residuals *Rp* and *Rwp* with values of 4.1 % and 5.6 %, respectively. The decrease in lattice parameter to 10.63713(8) Å indicates the substitution of Pt in the lattice. The absence of some reflections in the experimental data from calculated profile can be attributed to the synthesis of oxide by different methods and pretreatment.

The specific surface area of $Ce_2Zr_2O_7$, $Ce_2Zr_{1.96}Ru_{0.04}O_{7-\delta}$, $Ce_2Zr_{1.96}Pt_{0.04}O_{7-\delta}$ and $Ce_2Ti_{1.96}Pt_{0.04}O_{7-\delta}$ were found to be 35, 38, 42 and 40 (± 2) m^2/g. There is no marked difference in the surface area due to Ru substitution. However, for Pt substituted compounds there is slight increase in the surface area compared to the pristine oxide. This can be attributed to the higher number of exposed Pt compared to Ru.

3.1.2. X-ray photoelectron spectroscopy

Core level spectra of Ce 3d in $Ce_2Zr_{1.96}Pt_{0.04}O_{7-\delta}$, $Ce_2Zr_{1.96}Ru_{0.04}O_{7-\delta}$, and $Ce_2Ti_{1.96}Pt_{0.04}O_{7-\delta}$ are shown in Fig. 2a–c, respectively. The notations for the spectral components of Ce 3d are adopted from Burroughs et al. [32]. In the final state, the charge transfer occurs between Ce 4f levels and O 2p valence band. This results in $3d^94f^2$ O $2p^4$ (v^0) and $3d^94f^1$ O $2p^5$ (v') configurations for Ce^{3+}, while $3d^94f^2$ O $2p^4$ (v) and $3d^94f^1$ O $2p^5$ (v") configurations are observed for Ce^{4+} with a pure final state $3d^94f^0$ O $2p^6$ (v"'). A strong hybridization between these configurations gives rise to bonding and antibonding states leading to the formation of double peak spectra. Multiplet coupling does not result in formation of extra peaks in Ce 3d, however, broadening in spectral width is observed as a result of multiplet effect [32]. The binding energy and FWHM of the component peaks of Ce 3d are listed in Table 1. The ratio of Ce^{3+}:Ce^{4+} was calculated for $Ce_2Zr_{1.96}Pt_{0.04}O_{7-\delta}$ and it was found to be 0.45:0.55 before the reaction and 0.46:54 after the reaction. Thus, no significant change in the elemental states was seen after the reaction, which is indicative of the regeneration of the support sites. For $Ce_2Zr_{1.96}Ru_{0.04}O_{7-\delta}$, the ratio of Ce^{3+}:Ce^{4+} was changed from 0.51:0.48 to 0.45:0.55 after the reaction, indicating the oxidation Ce^{3+} to Ce^{4+} due to annihilation of oxide vacancies by CO_2. However, there is rise in Ce^{3+} state for $Ce_2Ti_{1.96}Pt_{0.04}O_{7-\delta}$, from the composition 0.54:0.45 to 0.58:0.42 after reaction. Due to existence of metastable states of these compounds, different composition of Ce^{3+} and Ce^{4+} states were observed for the synthesized samples [27,31].

XP spectra of Zr 3d in $Ce_2Zr_{1.96}Pt_{0.04}O_{7-\delta}$ and $Ce_2Zr_{1.96}Ru_{0.04}O_{7-\delta}$ recorded both before and after reaction are shown in Fig. 3a and b. The energy separation between Zr $3d_{5/2}$ and $3d_{3/2}$, due to spin-orbit splitting is 2.4 eV. The Gaussian broadening of the spin-orbit component and satellite peak is maintained as 1.25 eV and 3.5 eV, respectively [33]. Both the materials display the presence of Zr^{4+} with $3d_{5/2}$ peak at 182.2 eV. $Ce_2Zr_{1.96}Ru_{0.04}O_{7-\delta}$ manifest satellite peak at 186 eV, however, the satellite feature was absent in the spectra of $Ce_2Zr_{1.96}Pt_{0.04}O_{7-\delta}$. Morant et al. explained that the occurrence of satellite peaks might be ascribed to the metal-to-ligand charge transfer due to the presence of unoccupied 4d orbitals [33]. Zr 3d spectra displays slight shift in the binding energy to the higher value after reaction as a consequence of small change in particle size after reaction [34]. There was no change in the elemental composition of Zr even after the reaction for both the materials. As discussed by Arai et al., the presence of oxide vacancy near Zr ion does not affect its state and the charge is compensated by the change in oxidation state of Ce ion [31].

Fig. 3c shows the XP spectra of Ti 2p in $Ce_2Ti_{1.96}Pt_{0.04}O_{7-\delta}$ collected both before and after the reaction. In TiO_2, Ti $2p_{3/2}$ occurs at 458.5 eV,

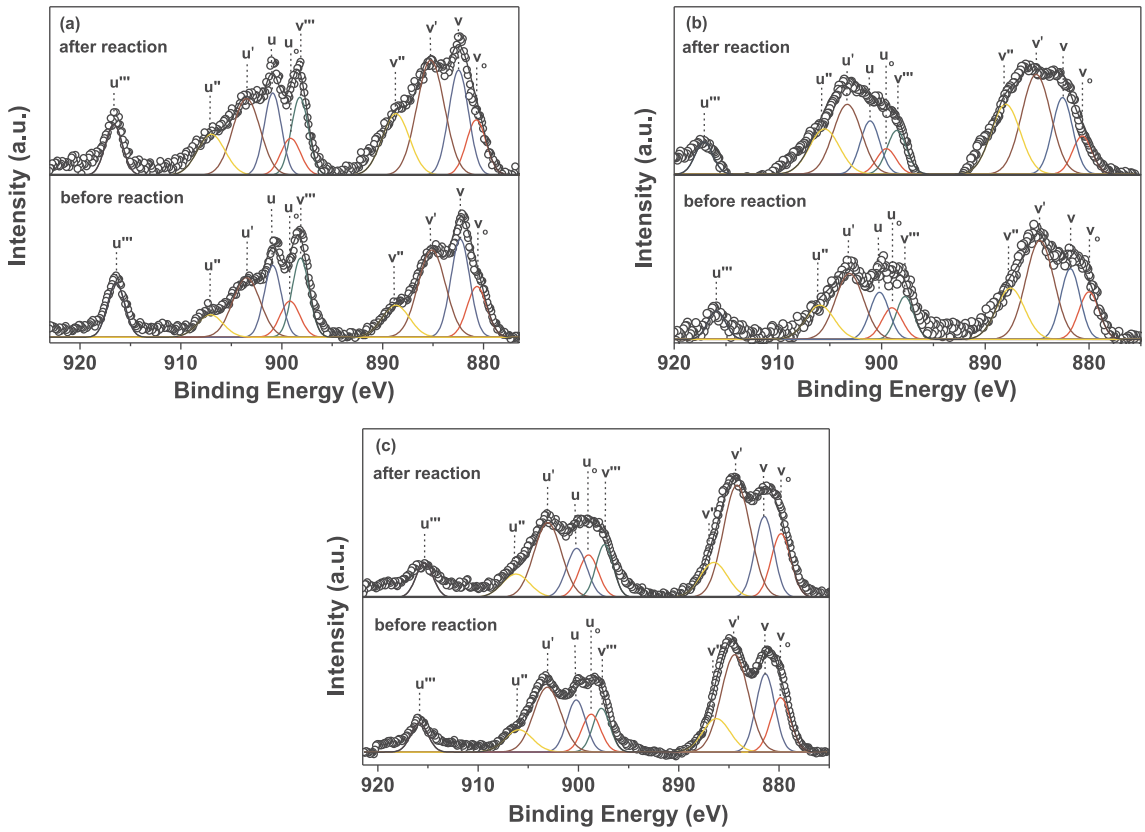

Fig. 2. XP spectra of Ce3d in (a) $Ce_2Zr_{1.96}Pt_{0.04}O_{7-\delta}$, (b) $Ce_2Zr_{1.96}Ru_{0.04}O_{7-\delta}$, (c) $Ce_2Ti_{1.96}Pt_{0.04}O_{7-\delta}$.

Table 1
Binding energy and FWHM of Ce 3d [35].

$3d_{5/2}$	Binding Energy	$3d_{3/2}$	Binding Energy	FWHM
v_o	880.2 ± 0.4	u_o	899.1 ± 0.2	2.0
v'	884.8 ± 0.4	u'	903.3 ± 0.3	3.0
v	881.9 ± 0.5	U	900.5 ± 0.4	2.0
v"	887.6 ± 0.8	u"	906.2 ± 0.6	3.2
v'''	897.9 ± 0.4	u'''	916.2 ± 0.6	3.2

however, in this study, Ti $2p_{3/2}$ was observed at 458.2 eV and the spin-orbit split was 5.6 eV [36]. The shift in the binding energy was observed due to development of lattice strain induced as a result of doping at Ti site [37]. As evident from the XP spectra, Ti $2p_{1/2}$ is broader and shorter than Ti $2p_{3/2}$ than expected. This can be attributed to the decay of core hole by Coster-Kronig process, which results in the Lorentzian broadening of the core electron line [38]. XP spectra indicate the presence of only Ti^{4+} in the synthesized sample. However, no change was observed in the electronic state of Ti after the reaction as CH_4 does not adsorb on the Ti site [39].

Fig. 4a depicts the XP spectra of Pt 4f in $Ce_2Zr_{1.96}Pt_{0.04}O_{7-\delta}$ acquired before and after reaction. Owing to spin-orbit splitting, the Pt 4f spectra split into $4f_{7/2}$ and $4f_{5/2}$ component with a separation of 3.1 eV. The binding energies of Pt $4f_{7/2}$ of Pt°, Pt^{2+} and Pt^{4+} states are 71, 72.4 and 74.4 eV, respectively. The linear background correction was performed and FWHM of 2 eV was maintained for all the component peaks [40]. The deconvoluted Pt 4f spectrum before reaction reveals the presence of Pt^{2+} and Pt^{4+} in the ratio of 0.87:0.13. However, Pt 4f spectrum of the spent catalyst showed the formation of Pt° state in conjunction with Pt^{2+} and Pt^{4+} state and the ratio of Pt°:Pt^{2+}:Pt^{4+} was found to be 0.43:0.42:0.15. Fig. 4c shows the XP spectra of Pt 4f in $Ce_2Ti_{1.96}Pt_{0.04}O_{7-\delta}$. It is evident from the spectra that Pt was present in metallic form in the synthesized material. The ratio of Pt°:Pt^{2+}:Pt^{4+} in the synthesized sample was 0.23:0.35:0.42, which changed to 0.41:0.48:0.11 after the reaction. The increase in metallic Pt after the reaction can be attributed to the presence of reducing atmosphere of CH_4 and H_2.

Fig. 4b shows the comparison of Ru $2p_{3/2}$ spectra of $Ce_2Zr_{1.96}Ru_{0.04}O_{7-\delta}$ before and after reaction. The binding energy of Ru $2p_{3/2}$ for Ru°, Ru^{4+} and Ru^{3+} is 459.2, 462.7 and 465, respectively. The satellite peaks is also noted for Ru^{4+} and Ru^{3+}. Morgan has performed detailed XPS characterization of Ru compounds and values of binding energy and FWHM is adopted from his work [41]. Ru $2p_{1/2}$ component is not shown here, due to the obscure nature of the spectra. The ratio of Ru°:Ru^{3+}:Ru^{4+} before the reaction was observed to be 0.15:0.53:0.32, while after the reaction the composition changes to 0.35:0.40:0.25. There was, however, an increase in the concentration of metallic Ru after the reaction that shows the involvement of Ru^{3+} and Ru^{4+} species. The uncertainty in Ru 3p (in $Ce_2Zr_{1.96}Ru_{0.04}O_{7-\delta}$) and Pt 4f (in $Ce_2Ti_{1.96}Pt_{0.04}O_{7-\delta}$) is high due to the obscure nature of the spectra.

3.1.3. Transmission electron microscopy

TEM was performed for $Ce_2Zr_{1.96}Pt_{0.04}O_{7-\delta}$, $Ce_2Zr_{1.96}Ru_{0.04}O_{7-\delta}$, and $Ce_2Ti_{1.96}Pt_{0.04}O_{7-\delta}$. Fig. 5a, e and i represents the bright field TEM images of $Ce_2Zr_{1.96}Pt_{0.04}O_{7-}$ δ, $Ce_2Zr_{1.96}Ru_{0.04}O_{7-\delta}$, and $Ce_2Ti_{1.96}Pt_{0.04}O_{7-\delta}$, respectively. Fig. 5m depicts the particle size distribution of $Ce_2Zr_{1.96}Pt_{0.04}O_{7-}$ δ and the average particle size of the synthesized samples was found to be ~ 10 nm. HRTEM micrographs demonstrate that the samples were highly crystalline in nature. Fig. 5b shows the HRTEM micrograph of $Ce_2Zr_{1.96}Pt_{0.04}O_{7-\delta}$ and its FFT analysis depicted in Fig. 5b inset and c revealed the presence of (222), (400) and (444) planes of the pyrochlore. The shift in the d-spacing might be due to the doping of Pt^{2+} ion in the lattice of $Ce_2Zr_2O_7$.

The electron diffraction pattern (Fig. 5d) confirmed the presence of various planes *i.e.* (222), (400), (440) and (444), which corroborates

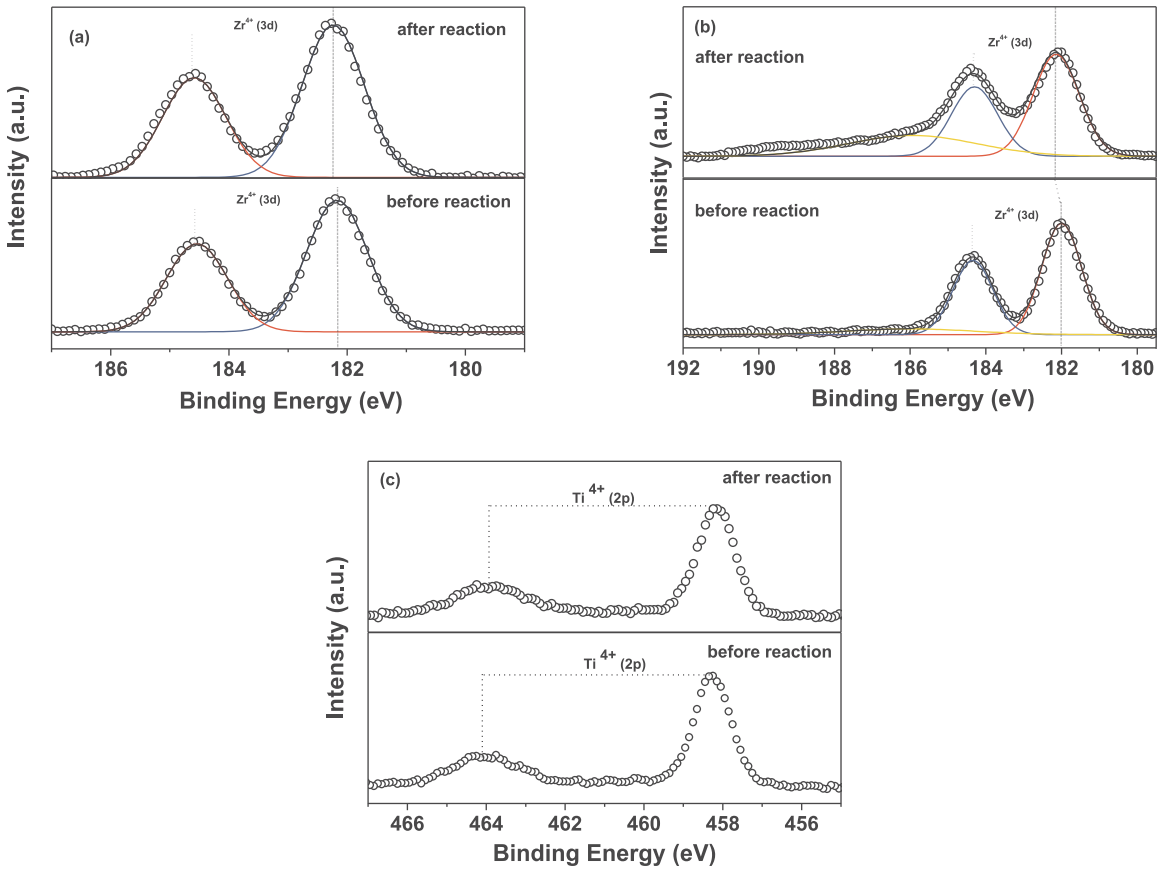

Fig. 3. XP spectra (a) Zr 3d in $Ce_2Zr_{1.96}Pt_{0.04}O_{7-\delta}$, (b) Zr 3d in $Ce_2Zr_{1.96}Ru_{0.04}O_{7-\delta}$, (c) Ti 2p in $Ce_2Ti_{1.96}Pt_{0.04}O_{7-\delta}$.

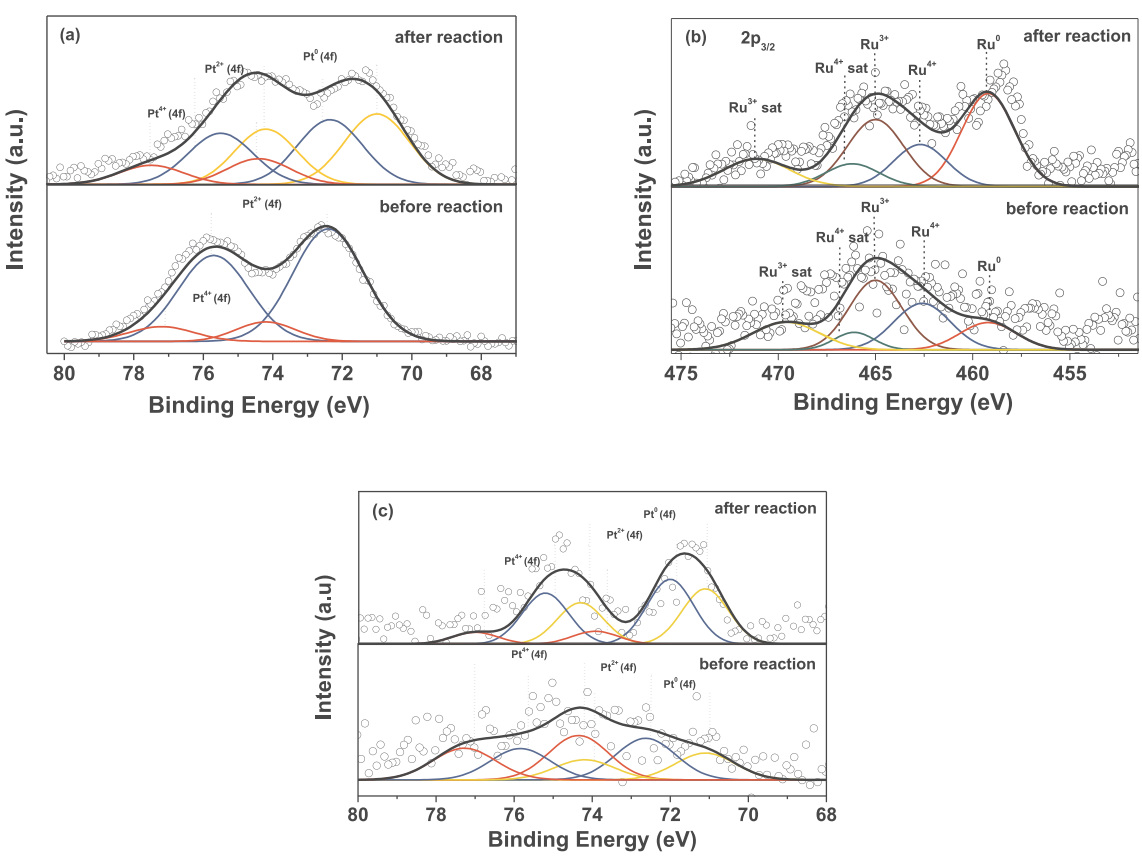

Fig. 4. XP spectra of (a) Pt 4f $Ce_2Zr_{1.96}Pt_{0.04}O_{7-\delta}$, (b) Ru 3p in $Ce_2Zr_{1.96}Ru_{0.04}O_{7-\delta}$, (c) Pt 4f in $Ce_2Ti_{1.96}Pt_{0.04}O_{7-\delta}$.

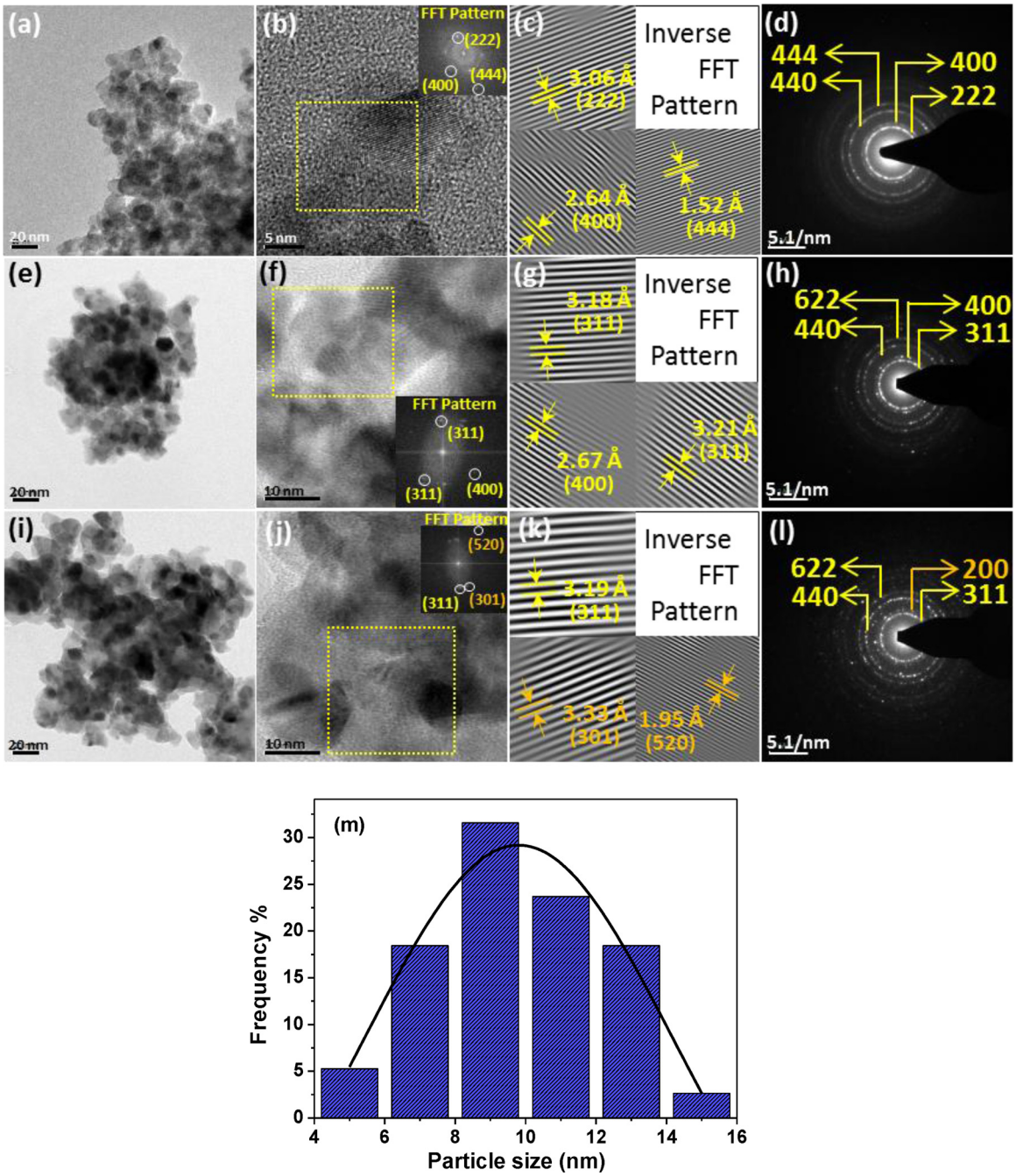

Fig. 5. TEM micrograph of $Ce_2Zr_{1.96}Pt_{0.04}O_{7-\delta}$: (a) Bright field images of (b) HRTEM micrograph, inset denotes the FFT pattern of the yellow marked region, (c) Inverse FFT pattern, (d) SAED pattern; TEM micrograph of $Ce_2Zr_{1.96}Ru_{0.04}O_{7-\delta}$: (e) Bright field images of (f) HRTEM micrograph, inset denotes the FFT pattern of the yellow marked region, (g) Inverse FFT pattern, (h) SAED pattern; TEM micrograph of $Ce_2Ti_{1.96}Pt_{0.04}O_{7-\delta}$: (i) Bright field images of (j) HRTEM micrograph, inset denotes the FFT pattern of the yellow marked region, (k) Inverse FFT pattern, (l) SAED pattern; (m) Particle size distribution of $Ce_2Zr_{1.96}Pt_{0.04}O_{7-\delta}$. (For interpretation of the references to colour in this figure legend, the reader is referred to the web version of this article.)

with the XRD result (Fig. 1a) [29]. However, no planes of CeO_2 and TiO_2 were observed in $Ce_2Zr_{1.96}Pt_{0.04}O_{7-\delta}$, indicating the presence of pure pyrochlore phase. HRTEM micrograph of $Ce_2Zr_{1.96}Ru_{0.04}O_{7-\delta}$ is shown in Fig. 5f and the inset represents the FFT pattern of selected yellow area. The inverse FFT pattern (Fig. 5g) of the spots shows the presence of pyrochlore planes *i.e.* (311) and (400). Fig. 5h depicts the SAED pattern of $Ce_2Zr_{1.96}Ru_{0.04}O_{7-\delta}$, representing the presence of (400), (311), (622) and (440) planes of pyrochlore. Fig. 5j shows the HRTEM micrograph $Ce_2Ti_{1.96}Pt_{0.04}O_{7-\delta}$ and the FFT pattern of the highlighted yellow region is depicted in the inset. The inverse FFT pattern (Fig. 5k) of the spots exhibited the presence of (311) plane of pyrochlore along with (301) and (520) plane of $Ce_2Zr_2O_8$. The SAED pattern of $Ce_2Ti_{1.96}Pt_{0.04}O_{7-\delta}$ (Fig. 5l) depicts the presence of (200) plane of CeO_2 in conjunction with (311), (440) and (622) planes of pyrochlores.

3.1.4. Inductively plasma coupled mass spectroscopy (ICP-MS)

The noble metal composition in pyrochlores was investigated using ICP-MS. The amount of Pt in $Ce_2Zr_{1.96}Pt_{0.04}O_{7-\delta}$ and $Ce_2Ti_{1.96}Pt_{0.04}O_{7-\delta}$ was found to be 3.17 and 3.03 at %, respectively, and Ru content in $Ce_2Zr_{1.96}Ru_{0.04}O_{7-\delta}$ was 3.77 at %.

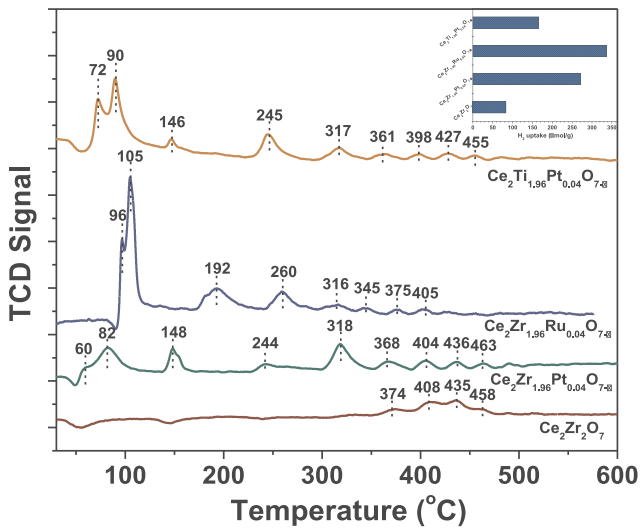

Fig. 6. TPR profile of the synthesized samples. The inset depicts the oxygen storage capacity of the samples.

3.2. H_2 temperature programmed reduction (H_2 TPR)

The effect of noble metal substitution in pyrochlore lattice was studied by H_2 TPR (Fig. 6). Substitution of metal in the oxide can lead to weakening of the metal oxygen bond in metal oxide and also H_2 activation at lower temperature can be achieved by the presence of noble metal. The metal atom at B site (dopant site) is coordinated by six oxygen atom, however, the coordination of the surface atom can vary between 1 – 5. It is evident from Fig. 6 that the reduction of $Ce_2Zr_2O_7$ occurs between 350 – 500 °C, similar observation was made by Baidya et al. [42]. TPR studies performed by Gaur et al. on 1% Ru substituted $La_2Zr_2O_7$ lattice, showed only one reduction peak at 280 °C, which was ascribed to the reduction of surface Ru species [21] Haynes et al. investigated the effect of Sr and Ru substitution in La and Zr site, respectively, and they observed two peaks at 182 and 555 °C. The appearance of peak at low temperature (182 °C) was attributed to the change in the chemical environment near Ru in the pyrochlore lattice [43]. In this study, the incorporation of Pt and Ru in the $Ce_2Zr_2O_7$ led to increase in reducibility of the support. Reduction for $Ce_2Zr_{1.96}Pt_{0.04}O_{7-\delta}$ began at temperature as low as 60 °C, which was assigned to the reduction of ionic Pt. The appearance of multiple reduction features in the TPR profile of $Ce_2Zr_{1.96}Pt_{0.04}O_{7-\delta}$ and $Ce_2Zr_{1.96}Ru_{0.04}O_{7-\delta}$ indicates the strong metal support interaction. A couple of intense peaks were observed for $Ce_2Zr_{1.96}Ru_{0.04}O_{7-\delta}$ at 96 and 105 °C. Similar feature were observed for Ru/Al_2O_3 by Haynes et al. and were ascribed to the reduction of RuO_x species to metallic Ru [43]. $Ce_2Ti_{1.96}Pt_{0.04}O_{7-\delta}$ showed similar reduction profile as $Ce_2Zr_{1.96}Pt_{0.04}O_{7-\delta}$ and $Ce_2Zr_{1.96}Ru_{0.04}O_{7-\delta}$, which indicates the formation of similar sites in Ce-pyrochlores. The comparison of TPR profiles of $Ce_2Zr_2O_7$ and $Ce_2Ti_2O_7$ is included in Fig. S1 in Supplementary information. Although, the reduction of $Ce_2Ti_2O_7$ occurs at higher temperature as compared to $Ce_2Zr_2O_7$, the H_2 uptake was higher in $Ce_2Ti_2O_7$ (135 μmol O/g). The H_2 uptake or oxygen storage capacity (OSC) of $Ce_2Zr_2O_7$, $Ce_2Zr_{1.96}Pt_{0.04}O_{7-\delta}$, $Ce_2Zr_{1.96}Ru_{0.04}O_{7-\delta}$ and $Ce_2Ti_{1.96}Pt_{0.04}O_{7-\delta}$ were found to be 83, 271, 337 and 166 μmol O/g, respectively. These values indicate that oxygen storage capacity of noble metal substituted catalyst is greatly enhanced by doping. However, the substitution of Pt in $Ce_2Ti_2O_7$ does not result in significant enhancement in OSC. H_2 uptake of these samples was not as high as the CeO_2-ZrO_2 catalyst reported in literature. Nonetheless, the reduction starts at lower temperatures in these catalysts indicating the ease of removal of lattice oxygen [22,25].

3.3. CO temperature programmed desorption (CO-TPD)

Substitution of noble metal in the lattice reduces the metal exposed at the surface of the catalyst and thus the amount of Pt at the surface of $Ce_2Zr_{1.96}Pt_{0.04}O_{7-\delta}$ was determined by CO TPD measurements. It is assumed that each mol Pt adsorbs one mol of CO molecule while calculating metal dispersion. The complexity in estimating the amount of CO adsorbed on Pt increases in substituted oxides. CO uptake by lattice oxygen increases in substituted oxides in comparison to the pristine oxide due to the weakening of metal oxygen bond, thus yielding higher CO desorption (shown in H_2-TPR studies). Fig. S3 (Supplementary information) shows that the desorption initiates immediately as the temperature is increased and this signal at low temperatures (< 100 °C) is attributed to the molecular desorption of CO from the Pt site. The features observed at higher temperature are assigned to the desorption of CO_2 as a result of oxidation of CO by lattice oxygen [44]. The amount of Pt exposed on the surface was calculated using the following relation [45],

$$\text{Dispersion} = \frac{V_m A_w 10^4}{W\% \, Sf}$$

where, V_m denotes the moles of CO per gram of sample, A_w is the atomic weight of metal, $W\%$ is the weight of metal in the sample and Sf is the stoichiometric factor indicating the molecules of CO per metal atom. The amount of exposed Pt atom on the surface of $Ce_2Zr_{1.96}Pt_{0.04}O_{7-\delta}$ was found to be 77 %. Turnover frequency was determined using the following formula

$$\text{TOF}\,(s^{-1}) = \frac{CH_4 \text{ conversion rate} \left(\frac{mol}{g_{cat}}/s\right)}{\text{Amount of CO desorbed from Pt} \left(\frac{mol}{g_{cat}}\right)}$$

3.4. Catalytic studies

3.4.1. Dry reforming of methane

DRM was studied over $Ce_2Zr_{1.96}Pt_{0.04}O_{7-\delta}$, $Ce_2Zr_{1.96}Ru_{0.04}O_{7-\delta}$ and $Ce_2Ti_{1.96}Pt_{0.04}O_{7-\delta}$ and the ratio of CH_4:CO_2 was maintained as 1:1 for all the samples (Fig. 7). Among all the samples, $Ce_2Zr_{1.96}Pt_{0.04}O_{7-\delta}$ showed highest conversion of CH_4 and CO_2 at all temperatures. $Ce_2Zr_{1.96}Pt_{0.04}O_{7-\delta}$ showed increase in conversion of CH_4 and CO_2 from 350 to 700 °C, however, $Ce_2Zr_{1.96}Ru_{0.04}O_{7-\delta}$ and $Ce_2Ti_{1.96}Pt_{0.04}O_{7-\delta}$ exhibited lower conversions up to 650 and 700 °C, respectively. The reason for low catalytic activity between 400 – 650 °C of $Ce_2Zr_{1.96}Ru_{0.04}O_{7-\delta}$ and $Ce_2Ti_{1.96}Pt_{0.04}O_{7-\delta}$ might be attributed to the accumulation of active carbon or CH_x species formed by CH_4 dissociation. With further increase in temperature the desorption of these species will result in the availability of these sites for adsorption and activation of oxidant (CO_2) leading to increase in conversion at higher temperature. $Ce_2Ti_{1.96}Pt_{0.04}O_{7-\delta}$ and $Ce_2Zr_{1.96}Ru_{0.04}O_{7-\delta}$ showed 7.1 % and 14.6 % CH_4 conversion at 600 °C, respectively, whereas $Ce_2Zr_{1.96}Pt_{0.04}O_{7-\delta}$ exhibited 90.8 % CH_4 conversion. Nearly, 97.6 % and 96.4 % CH_4 conversion was obtained at 650 and 800 °C for $Ce_2Zr_{1.96}Pt_{0.04}O_{7-\delta}$ and $Ce_2Zr_{1.96}Ru_{0.04}O_{7-\delta}$, respectively. However, only 85 % CH_4 conversion was observed for $Ce_2Ti_{1.96}Pt_{0.04}O_{7-\delta}$ at 850 °C. The low catalytic activity of $Ce_2Ti_{1.96}Pt_{0.04}O_{7-\delta}$ can be due to the low oxygen storage capacity compared to noble metal substituted $Ce_2Zr_2O_7$. Furthermore, the presence of metallic Pt on the surface of $Ce_2Ti_{1.96}Pt_{0.04}O_{7-\delta}$ can cause sintering of Pt at higher temperature. For $Ce_2Zr_{1.96}Pt_{0.04}O_{7-\delta}$ and $Ce_2Zr_{1.96}Ru_{0.04}O_{7-\delta}$, the CH_4 conversion was higher than the CO_2 conversions for temperatures below 600 °C, indicating the occurrence of reverse water gas shift reaction (RWGS). $Ce_2Ti_{1.96}Pt_{0.04}O_{7-\delta}$ showed similar conversion of CH_4 and CO_2, representing very low rate of RWGS. Noble metal substituted $Ce_2Zr_2O_7$ compounds exhibited higher catalytic activity that Pt substituted $Ce_2Ti_2O_7$, demonstrating strong metal-support interaction between

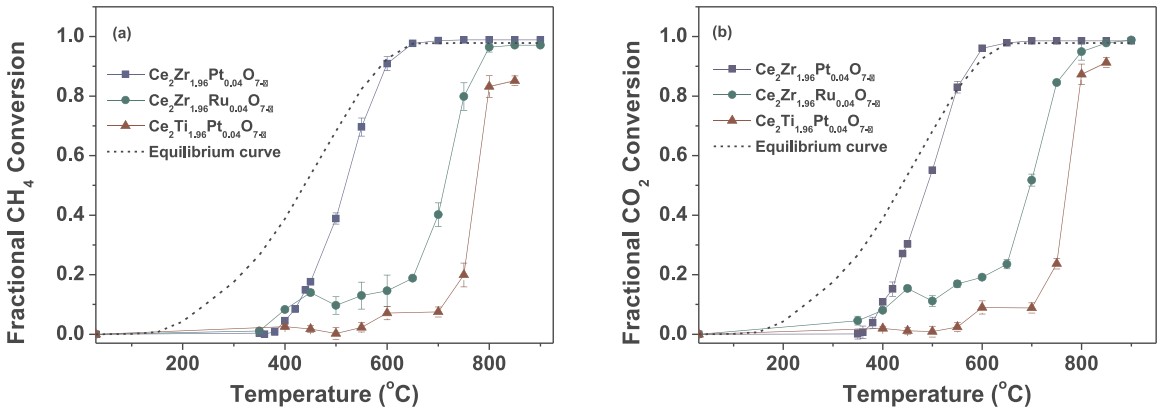

Fig. 7. Variation of fractional conversion with temperature of $Ce_2Zr_{1.96}Pt_{0.04}O_{7-\delta}$, $Ce_2Zr_{1.96}Ru_{0.04}O_{7-\delta}$ and $Ce_2Ti_{1.96}Pt_{0.04}O_{7-\delta}$ (a) CH_4, (b) CO_2; Reaction conditions- CH_4:CO_2 - 3:3, GHSV = 38,120 h^{-1}.

noble metal and $Ce_2Zr_2O_7$. Amongst all the samples, $Ce_2Zr_{1.96}Pt_{0.04}O_{7-\delta}$ exhibited highest catalytic activity towards DRM and hence, further studies were performed on it. The catalytic studies were also performed at 20 % CH_4 retaining the reactant gas (CH_4:CO_2) ratio as 1 and the comparison of conversion and reaction rates of CH_4 and CO_2 is included in Supplementary information (Fig. S4). The catalytic activity of $Ce_2Zr_{1.96}Pt_{0.04}O_{7-\delta}$ was compared with 4% Pt/ $Ce_2Zr_2O_7$ towards DRM and it was observed that Pt-substituted $Ce_2Zr_2O_7$ exhibited significantly higher catalytic activity compared to Pt impregnated over $Ce_2Zr_2O_7$ (Fig. S5, Supplementary information).

Fig. 11a shows the concentration profiles of various species at the reactor outlet during DRM reaction over $Ce_2Zr_{1.96}Pt_{0.04}O_{7-\delta}$. The rate of formation of H_2 was higher than CO up to 550 °C as a consequence of methane decomposition and Boudouard reaction. Above 550 °C, the increase in CO might be due to the occurrence of RWGS or oxidation of carbon deposited on the catalyst surface. The water formed as a result of RWGS can also oxidize the carbon deposited on catalyst surface [19]. A small increase in concentration of CO_2 and low concentration of CO was observed at temperature below 350 °C, which could be due to RWGS. However, the effect of these reactions disappeared after 650 °C, indicating the selectivity of the catalyst towards DRM. Syngas ratio (H_2/CO) plays a vital role in determining the process employed for its conversion into value added products. Fig. 11f shows the syngas ratio for $Ce_2Zr_{1.96}Pt_{0.04}O_{7-\delta}$, calculated at different temperatures for different reforming routes. The H_2/CO ratio was determined at various temperatures for $Ce_2Zr_{1.96}Pt_{0.04}O_{7-\delta}$ and it was observed that the ratio was constant at 0.84 after 650 °C.

Fig. 8 displays the influence of Pt loading on catalytic activity of $Ce_2Zr_{2-x}Pt_xO_{7-\delta}$ (x = 0.02, 0.04, 0.06) towards DRM. It was observed that $Ce_2Zr_{1.98}Pt_{0.02}O_{7-\delta}$ showed decrease in catalytic activity at lower temperature (< 600 °C), whereas the conversions increases with rise in temperature for $Ce_2Zr_{1.96}Pt_{0.04}O_{7-\delta}$. Further increasing the Pt loading to 6 at% had no significant effect on conversions. T99% of CH_4 for $Ce_2Zr_{1.96}Pt_{0.04}O_{7-\delta}$ and $Ce_2Zr_{1.94}Pt_{0.06}O_{7-\delta}$ were found to be 700 °C and 800 °C, respectively, whereas $Ce_2Zr_{1.98}Pt_{0.02}O_{7-\delta}$ showed a maximum of 92 % conversion at 800 °C. The increase in activity was expected as the Pt doping percentage was increased. Besides, increasing the number of active sites (Pt), the increase in dopant concentration leads to the formation of defects like oxide vacancies, which is favorable for CO_2 activation. However, on further increasing concentration of Pt to 6%, there was no increase in the conversion of CH_4 and CO_2. This can be explained by (a) an incomplete substitution of the Pt atom in the oxide lattice resulting in deactivation due to C-deposition, or (b) the possibility of formation of more complex defects upon increasing the dopant concentration, which reduces the number of free vacancy concentration [46].

The effect of doping of Pt on Ce (A) and Zr (B) site on the catalytic activity towards DRM was also investigated (Fig. 9). Substitution of Pt at the B site (Zr^{4+}) exhibited higher DRM activity than that of Pt substituted at the A site. This can be illustrated by the formation of anionic defects and the difference in the ionic radii of the dopant. Firstly, the doping of Pt^{2+} at Ce site leads to the creation of lesser number of oxide vacancies as compared to doping of Pt^{2+} at Zr site to maintain charge neutrality. Secondly, the difference in the ionic radii of the Ce^{3+} (1.28 Å) and Pt^{2+} (0.94 Å) is higher than the difference in Zr^{4+} (0.86 Å) and Pt^{2+}, making substitution of Pt arduous at Ce site. Butler et al. suggested that the ionic radii of the dopant strongly influence the binding energy of the associated defects, which can be

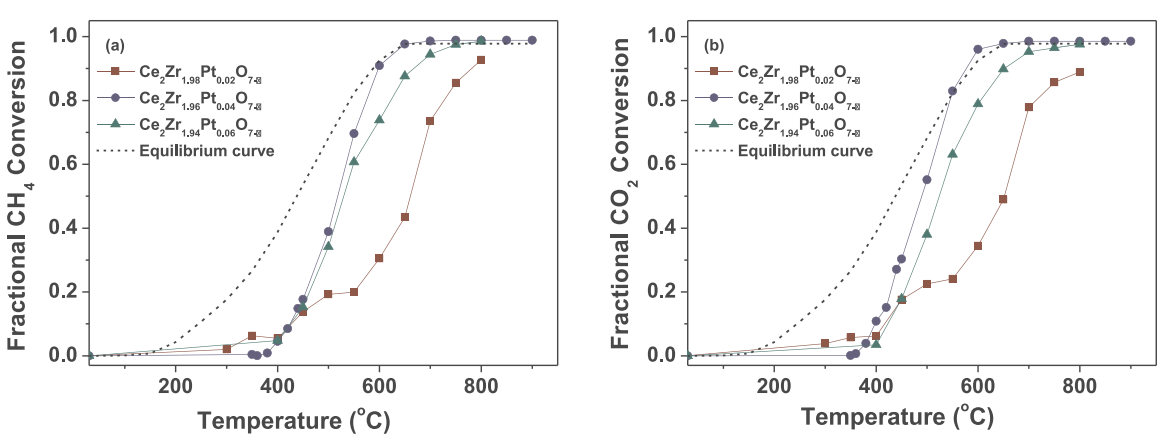

Fig. 8. Effect of Pt doping % in $Ce_2Zr_{1.96}Pt_{0.04}O_{7-\delta}$ on fractional conversion with temperature (a) CH_4, (b) CO_2; Reaction conditions- CH_4:CO_2 - 3:3, GHSV = 38,120 h^{-1}.

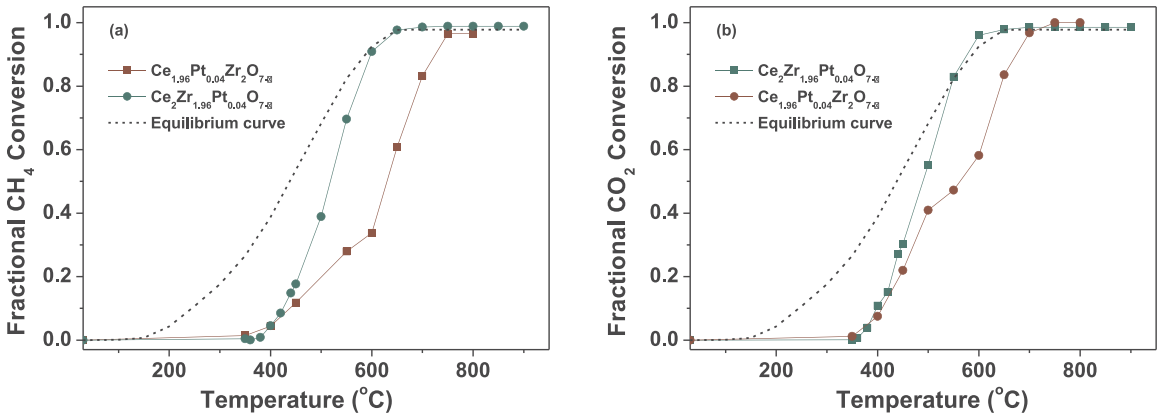

Fig. 9. Effect of Pt doping position in $Ce_2Zr_{1.96}Pt_{0.04}O_{7-\delta}$ on fractional conversion with temperature (a) CH_4, (b) CO_2; Reaction conditions- CH_4:CO_2 - 3:3, GHSV = 38,120 h^{-1}.

minimized if the ionic radii of dopant is close to that of parent ion [47]. The reduction studies by H_2 over these materials indicate the doping of Pt at Ce did not have increase in OSC of the material (Fig. S2, in Supplementary information). Therefore, $Ce_2Zr_2O_7$ pyrochlores with Pt substitution on the Zr site exhibited increased catalytic activity towards DRM.

Fig. 10a and b shows the variation in conversion of CH_4 and CO_2 with W/F_{CH_4} and W/F_{CO_2} at different temperature for $Ce_2Zr_{1.96}Pt_{0.04}O_{7-\delta}$. These studies were performed to find the kinetic regime in the differential reactor. The reaction rate at various temperatures was determined by the slope of the plot (initial linear region) and was calculated using $r_{CH_4} = F_{CH_4}\frac{X_{CH_4}}{W}$, where W is the weight of the catalyst and F_{CH_4} is the molar flow rate of CH_4. The apparent activation energy was determined by Arrhenius plot using the rates calculated from Fig. 10a and b. The apparent activation energies for $Ce_2Zr_{1.96}Pt_{0.04}O_{7-\delta}$ as shown in Fig. 10c were found to be 146 ± 5 kJ/mol for CH_4 and 112 ± 4 kJ/mol for CO_2. At 700 °C, the yield of H_2 and CO for $Ce_2Zr_{1.96}Pt_{0.04}O_{7-\delta}$ was found to be 77.7 % and 94.5 %, respectively. Table 2 exhibits the comparison of rates, TOF and apparent activation energy over different catalysts reported in the literature with respect to the samples reported in this study.

3.4.2. Partial oxidation and autothermal reforming of methane

$Ce_2Zr_{1.96}Pt_{0.04}O_{7-\delta}$ was studied for partial oxidation of methane with CH_4:O_2 as 1:0.5. Fig. 11b depicts the concentration of various species obtained at the exit of the reactor. CO_2 formation was observed

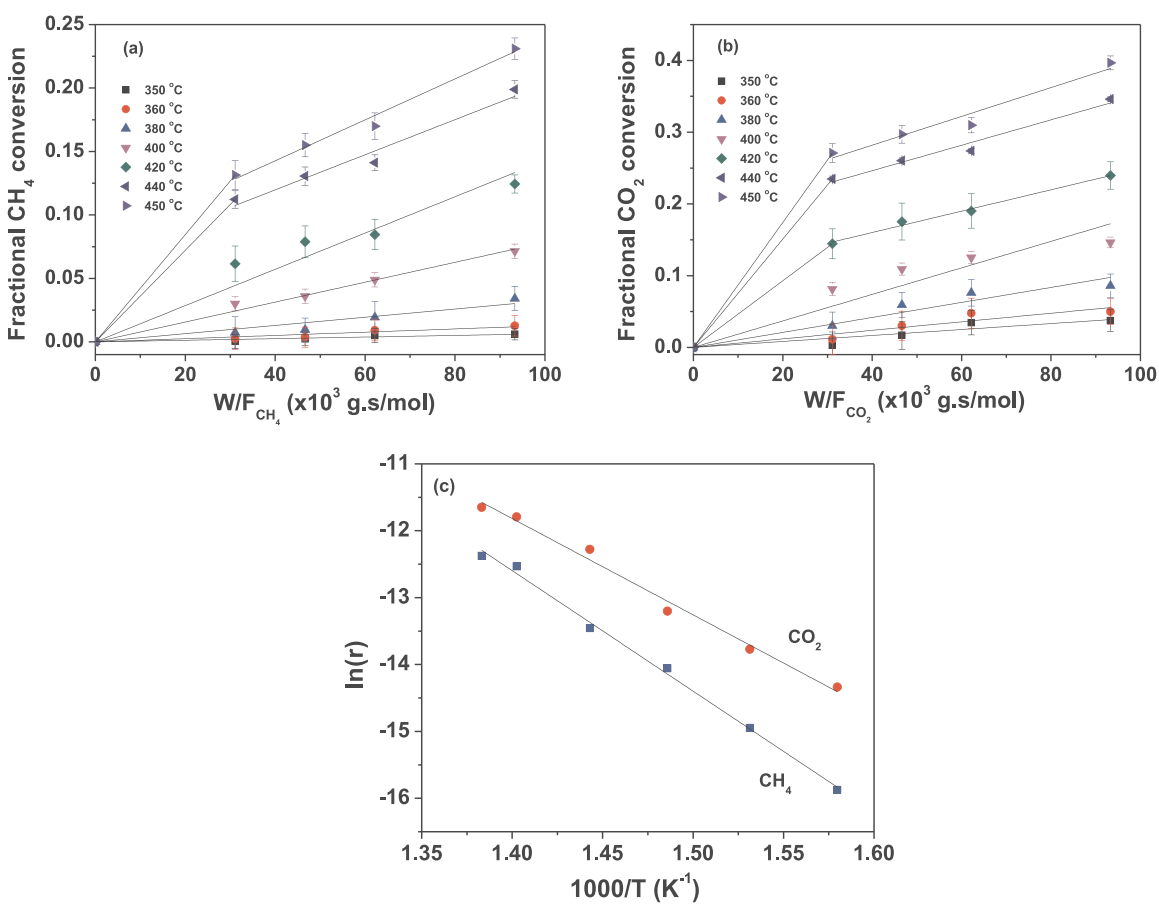

Fig. 10. Variation of fractional conversion with W/F for $Ce_2Zr_{1.96}Pt_{0.04}O_{7-\delta}$ (a) CH_4, (b) CO_2, (c) Arrhenius plot.

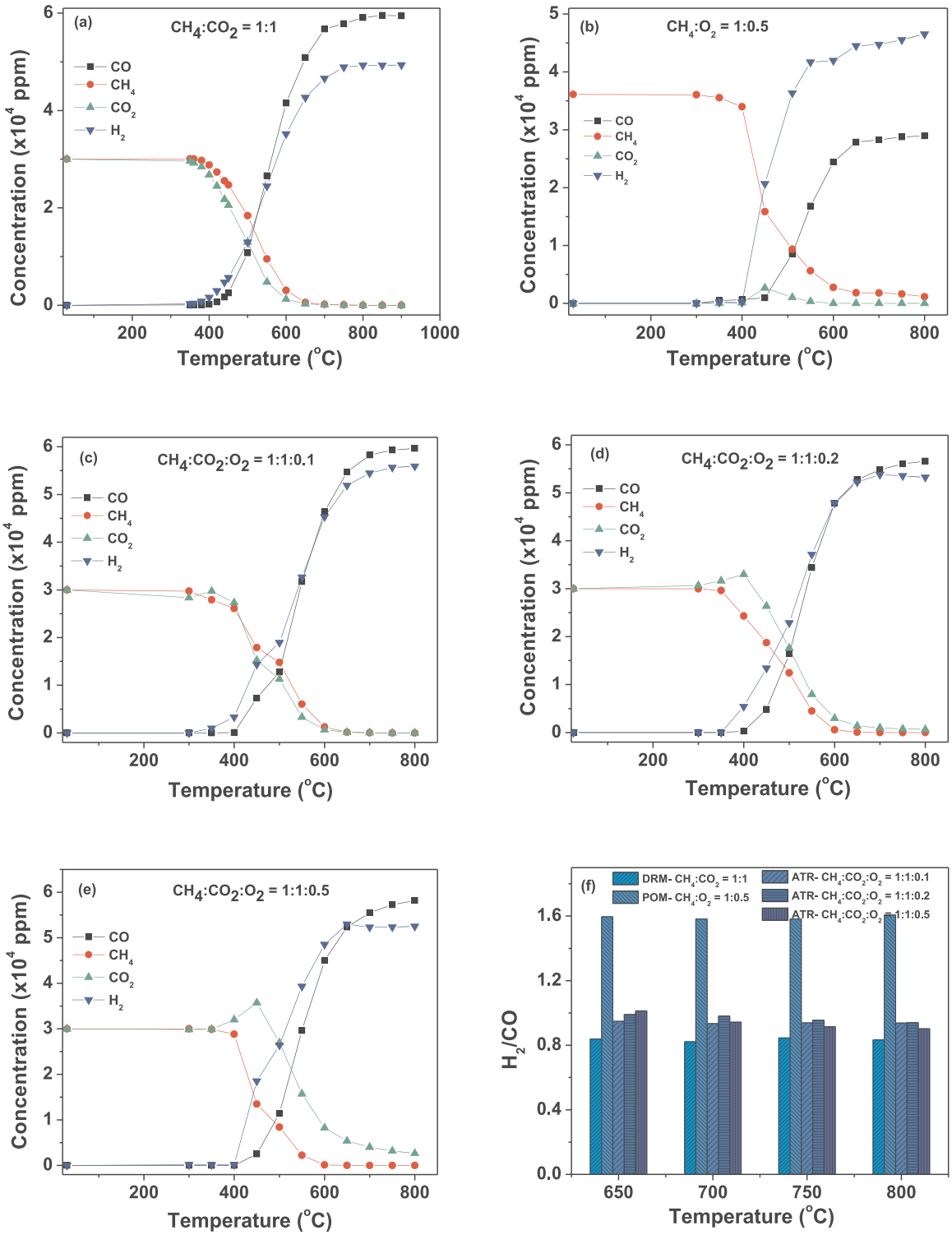

Fig. 11. Variation of gas concentration with temperature on $Ce_2Zr_{1.96}Pt_{0.04}O_{7-\delta}$ for (a) DRM; (b) POM; ATR (c) CH_4:CO_2:O_2 – 1:1:1:0.1, (d) CH_4:CO_2:O_2 – 1:1:1:0.2, (e) CH_4:CO_2:O_2 – 1:1:1:0.5; (f) Variation of H_2/CO for various reforming reaction.

between 400 – 600 °C due to RWGS and total oxidation of methane. However, as the temperature was raised, the rate of formation of CO increased. The H_2/CO ratio is expected to be close to 2 for POM and in the present study the H_2/CO ratio for POM was found to be ~1.60 above 650 °C (Fig. 11f). Autothermal reforming of methane was performed over $Ce_2Zr_{1.96}Pt_{0.04}O_{7-\delta}$ at three different composition of O_2 with CH_4:CO_2:O_2 as 1:1:0.1, 1:1:0.2 and 1:1:0.5. It is evident from Fig. 11c–e that with increasing concentration of O_2, the formation of CO_2 increased between 350 – 600 °C. This indicates that the extent of side reaction like total oxidation of methane and RWGS also increased. Fig. 11f shows the H_2/CO ratio at different temperatures for DRM, POM and ATR (with different O_2 concentration). H_2/CO ratio for DRM above 650 °C was 0.84, which then improved to 0.94 with the introduction of 0.6 % of O_2 in the feed. It is thus apparent from this study that by varying the reactant concentration in ATR, H_2/CO ratio can be tuned, which is in agreement with the previous studies [52,53].

Table 2
Comparison of catalytic results with the literature.

Catalyst	$E^{a}_{CH_4}$ (kJ/mol)	$E^{a}_{CO_2}$ (kJ/mol)	Rate (μmol/g/s)	TOF (s^{-1})	Carbon (wt%)	Nature of carbon	Ref
5 wt% $Ni/Ce_{0.8}Pr_{0.2}O_2$			4.35 (550)[b,a]	5.0 (550)	29.9 (25)[c,b]	Filamentous	[23]
2 wt% Ru sub[c]-$La_2Zr_2O_7$	60	105	–	–	5 (10)	Graphitic	[48]
3.78 wt% Pt sub-$La_2Zr_2O_7$	152	48	–	–	negligible	–	[48]
$Ni/CeO_2(44)/ZrO_2(56)$	69	–	–	–	4.1	Filamentous	[25]
NiCe/SBA-16	–	–	–	15.7 (700)	3.8 (100)	filamentous, amorphous	[5]
0.4 wt% Rh/Al_2O_3	111	–	–	4.2 (850)	–	–	[49]
$LaNiO_3$	68	77	130 (700)	–	–	–	[50]
$LaNiO_3/CeSiO_2$			43.3 (800)	0.63 (800)	0.76 (24)	–	[51]
$Ce_2Zr_{1.96}Pt_{0.04}O_{7-\delta}$ [d]	146	112	48.4 (500)	2.5 (500)	3.2 (24)	amorphous, graphitic	This work

[a] Temperature in °C in parentheses.
[b] Time on stream in h in parentheses.
[c] Substituted.
[d] Values are reported for feed- 20 % CH_4/20 % CO_2.

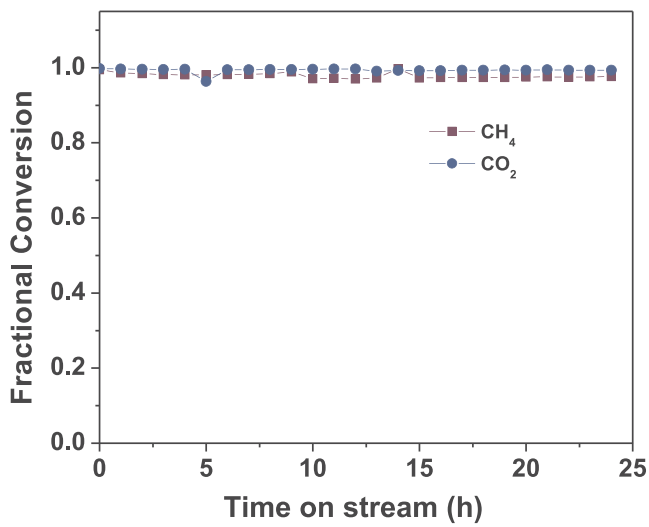

Fig. 12. Time on stream CH_4 and CO_2 conversion for dry reforming of methane on $Ce_2Zr_{1.96}Pt_{0.04}O_{7-\delta}$.

3.5. Stability studies

The time on stream studies was performed for 24 h on $Ce_2Zr_{1.96}Pt_{0.04}O_{7-\delta}$ to investigate the stability of the catalyst. Fig. 12 depicts the excellent stability of the catalyst with no sign of deactivation for the continuous cycle. To study the amount of coke deposited over the spent catalyst TGA was performed under N_2 flow, which upon evaluation was found to be 1.5 wt% for 3% CH_4 with CH_4:CO_2 maintained as 1. The stability studies were also performed at 20 %. CH_4 concentration (CH_4:CO_2 – 1) and the catalyst showed high stability for period of 24 h with 3.2 wt% of deposited carbon. Table 2 depicts the comparison of coke deposition over different catalysts after time on stream studies.

TEM micrographs were recorded subsequent the stability studies of $Ce_2Zr_{1.96}Pt_{0.04}O_{7-\delta}$, to gain insight in the effect of reaction condition on the catalyst structure and the nature of carbon deposited. Fig. 13a displays the bright field TEM image of the spent catalyst, which exhibits no significant change in the particle size after the reaction. Additionally, the presence of amorphous layer of carbon over the catalyst surface (marked with pink arrow) was noted and was marked as region A in Fig. 13a. The electron diffraction pattern of region A is depicted in Fig. 13d. Due to the amorphous layer of carbon, only few Laue rings were seen that corresponds to (222) and (400) planes of $Ce_2Zr_2O_7$ (shown in yellow) and (400) and (531) planes of $Ce_2Zr_2O_8$ ((shown in orange). Fig. 13b exhibits the HRTEM micrograph of the spent catalyst and inset denotes the FFT pattern of the marked yellow region. The inverse FFT pattern shown in Fig. 13c reveals the presence of (333) and (620) planes of pyrochlore along with $(31\overline{2})$ plane of $Ce_2Zr_2O_8$. Additionally, the deposition of (111) plane of graphitic carbon (denoted in white) was also observed. The electron diffraction pattern (Fig. 13e) recorded from region B reveals high crystallinity. Different planes of $Ce_2Zr_2O_7$ - (311), (440), (622) were observed along with (400) plane of $Ce_2Zr_2O_8$.

3.6. In situ FTIR (DRIFTS) studies on $Ce_2Zr_{1.96}Pt_{0.04}O_{7-\delta}$

DRIFTS study was performed on $Ce_2Zr_{1.96}Pt_{0.04}O_{7-\delta}$ for DRM, POM and ATR at different temperatures *i.e.* 30, 350, 450 and 600 °C. The shown spectra were recorded once the peak intensities attained stable values (~30 min.). The bands at 3728 and 3687 cm^{-1} correspond to −OH group bonded to the surface, whose intensity decreased with increasing temperature. At temperature above 350 °C, the presence of −OH species can be attributed to the dissociation of H_2O formed via RWGS. All the spectra (Figs. 14 and 15) exhibited the presence of gaseous CH_4 at 3016 (ν_3) and 1305 cm^{-1} (ν_4) and gaseous CO_2 at 2360 and 2344 cm^{-1}. It is to be noted that the bands at 2917 cm^{-1} (ν_1) and 1533 cm^{-1} (ν_2) were absent at room temperature as they are infrared inactive due to symmetrical structure of CH_4 [54]. Fig. 15a shows the formation of Pt−CO band at 2058 and 2036 cm^{-1} and gaseous CO at 2172 and 2112 cm^{-1} at temperature as low as 350 °C for DRM. The shift in frequency of Pt−CO band can be attributed to the co-adsorption of CO and CH_4 on Pt. This can be clearly seen in Fig. S6 d in Supplementary information, where the IR spectra were recorded in the presence of CH_4 and CO at different temperatures. The intensity of gaseous CO band increased with temperature indicating the low extent of Boudouard reaction on the catalyst surface. However, the gaseous CO band for POM (Fig. 15b) and ATR (Fig. 15c) was apparent only at higher temperature. It is evident from the spectra that no bands were observed at 2163 and 2169 cm^{-1}, which corresponds to CO adsorption on Ce^{3+} and Ce^{4+} [55]. Fig. 15b (POM) and 15c (ATR) shows the presence of adsorbed CO_2 band even at higher temperature due to the oxidation of CO in the presence of oxygen.

A fluctuating band was observed in the region 2893 − 3152 cm^{-1} with a sharp characteristic mode of gaseous CH_4 at 3017 cm^{-1} (ν_3) in all reforming processes (Fig. 14). However, the small peaks at 2975 and 2875 cm^{-1} appeared at higher temperatures, which were assigned to CH_4 adsorbed on Pt. These bands arise due to red shift in gaseous CH_4 band at 3017 and 2917 cm^{-1}, as a consequence of CH_4 adsorption on Pt. The vibrational mode at 2917 cm^{-1} (ν_1) is forbidden in infrared due to T_d symmetry of the CH_4. However, the strong interaction of CH_4 molecule with the catalyst surface leads to lower symmetry structure like $C_{3\nu}$, which can be seen with the red shift in ν_1 band at 2875 cm^{-1} [54,56]. The oscillating band was noticed on the either side of the ν_3 in all the spectra. Munera et al. observed a similar kind of spectra on

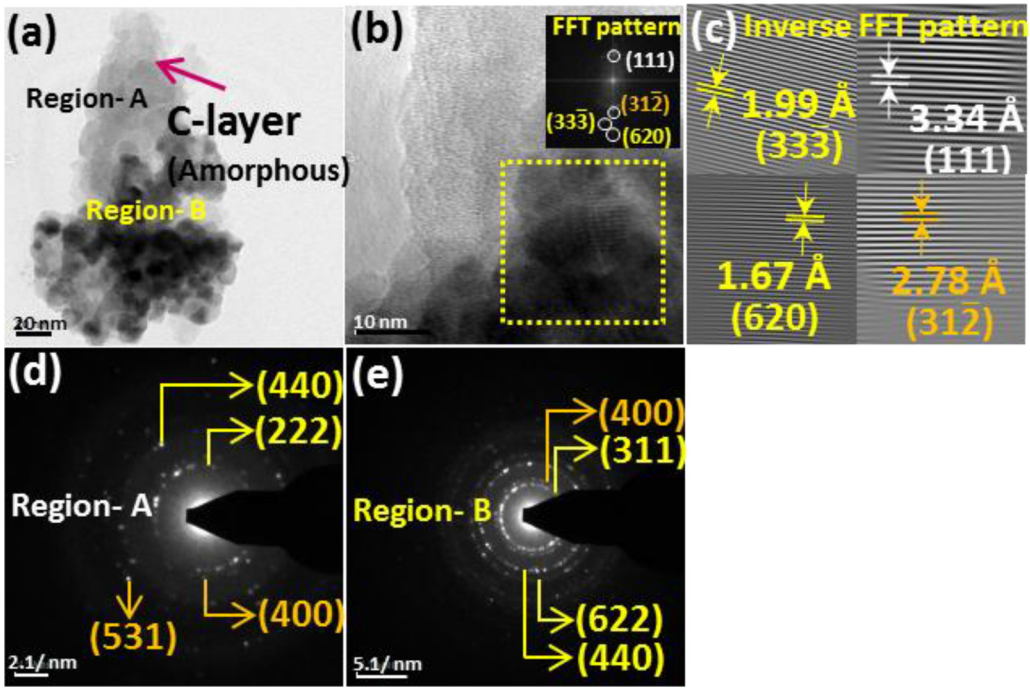

Fig. 13. TEM micrographs of $Ce_2Zr_{1.96}Pt_{0.04}O_{7-\delta}$ recorded after stability studies (a) Bright field TEM image showing amorphous carbon (shown by pink arrow), (b) HRTEM micrograph, inset represents FFT pattern yellow marked region, (c) Inverse FFT pattern, (d) and (e) SAED pattern from Region A and B, respectively. (For interpretation of the references to colour in this figure legend, the reader is referred to the web version of this article.)

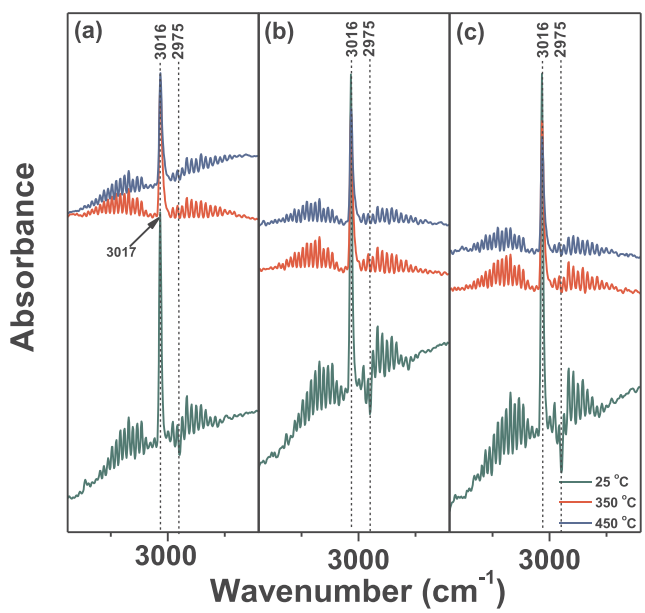

Fig. 14. C—H stretching band at different temperature on $Ce_2Zr_{1.96}Pt_{0.04}O_{7-\delta}$ for (a) DRM, (b) POM, (c) ATR, CH_4:CO_2:O_2 – 1:1:1:0.5.

La_2O_3 in the presence of CO_2 and CH_4 [57] The reasons for the oscillating nature of the spectra in this region are: (a) at low temperatures, these oscillations are seen due to the interaction of CH_4 with the hydroxyl group on the surface. The interaction of CH_4 with hydroxyl species induces dipole moment in CH_4, which causes the ν_1 mode (symmetric stretch) to become weakly active [58], (b) at high temperature, the occurrence of these bands is probably due to the interaction of CH_4 with the surface species like formates, carbonates or adsorbed hydrogen, (c) there is also possibility of occurrence of C—H vibration of formates in the range of 2950 – 2800 cm^{-1} [59]. As the above mentioned interactions are weak in nature, when the system is purged with N_2, no bands were seen in this range. This also suggests that CH_x bands were absent.

In the region 1700 – 1000 cm^{-1}, multiple bands were observed which are attributed to carbonate, formyl and formate species (Fig. 16). Heyl et al. [60] reported that the band due to C=O stretching of formyl species was observed at 1780 cm^{-1} on Rh catalysts, whereas, Chafik et al. [61] observed the same band at 1635 cm^{-1}. In the present case, there were no bands in these regions indicating the absence of formyl species. This confirms that the CH_x species were not formed over the surface of $Ce_2Zr_{1.96}Pt_{0.04}O_{7-\delta}$. To distinguish between carbonate and formate bands, the spectra were recorded in the presence of CH_4 and CO_2 alone (Fig. S6a–c in Supplementary information). Formate species appears between 1510 – 1550 cm^{-1} (ν_{OCO}^{asym}), 1310 – 1375 cm^{-1} (ν_{OCO}^{sym}) and 1088 cm^{-1}, whereas carbonate vibrational bands were observed at 1550, 1464 and 1088 cm^{-1} [59,61,62]. It is thus apparent that (Fig. S6a–c) that not only carbonate species decomposes as the temperature is increased, but also different types of formate species were formed.

4. Kinetic and mechanism development on $Ce_2Zr_{1.96}Pt_{0.04}O_{7-\delta}$

Noble metal are highly active for dry reforming of methane and their activity declines in the following order Ru > Rh > Ni ~ Ir > Pt > Pd, while the coke formation decreases in the order of Ni > > Pt > Ru [63,64]. Platinum group metals are responsible for the activation of C-H bond in methane and also enhance the spillover of hydrogen and oxygen species between metal support [3]. However, in the present study, Pt-substituted oxide exhibited better catalytic activity than the Ru catalysts. This result prompts that the support plays a crucial role in not just controlling coke deposition but also in modifying the stability of various surface intermediates [12,65]. Previous studies on DRM revealed that the C—H bond activation is the only rate controlling step over supported metal [66]. Although, there are few studies, where, the adsorption of CO_2 is also considered as kinetically-relevant [67]. Vasiliades et al. demonstrated with the help of SSTIKA studies that the oxidation of carbon occurs by lattice oxygen over Ni/$Ce_{0.38}Zr_{0.62}O_{2-\delta}$ and that the carbonate type species are inactive for the reaction [22]. However, studies on La_2O_3 support showed the formation of oxycarbonates and gasification of carbon by carbonate formation was found to be rate determining step [68,69]. Pakhare et al. proposed a dual-site mechanism for Rh-substituted $La_2Zr_2O_7$ pyrochlores, with CH_4 activation being the rate determining step. However, the participation of formates and carbonate species were not considered in the

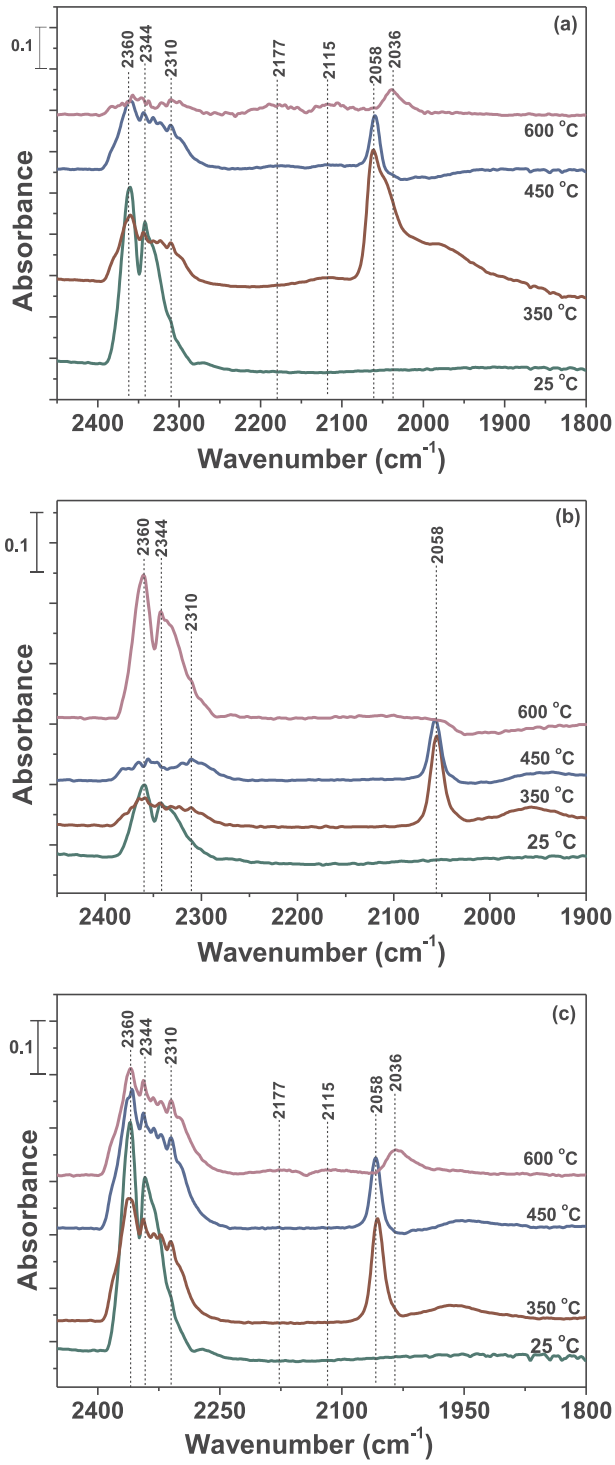

Fig. 15. DRIFT spectra recorded at different temperature on $Ce_2Zr_{1.96}Pt_{0.04}O_{7-\delta}$ in the region 2450–1800 cm^{-1} for (a) DRM, (b) POM, (c) ATR, CH_4:CO_2:O_2 – 1:1:1:0.5.

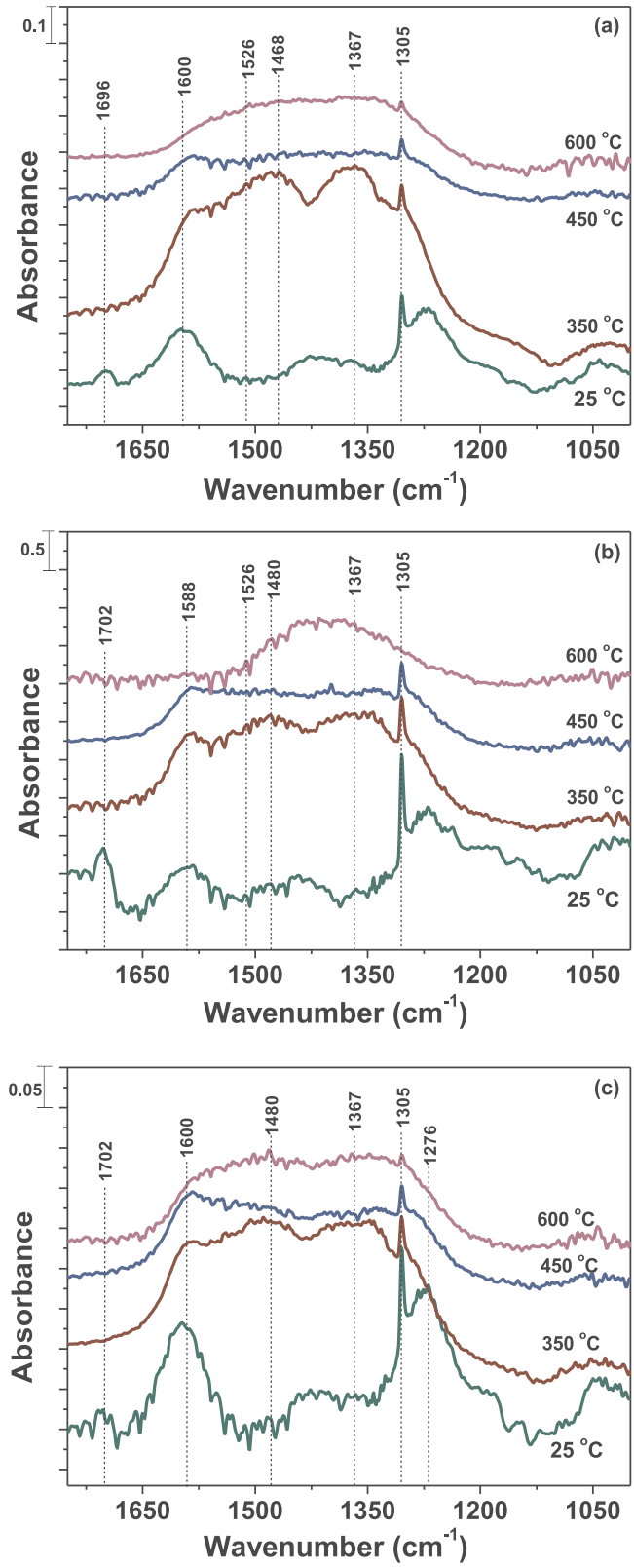

Fig. 16. DRIFT spectra recorded at different temperature on $Ce_2Zr_{1.96}Pt_{0.04}O_{7-\delta}$ in the region 1750–1000 cm^{-1} for (a) DRM, (b) POM, (c) ATR, CH_4:CO_2:O_2 – 1:1:1:0.5.

mechanism [19].

There are many studies on the mechanistic and kinetic study of DRM where Eley-Rideal and Langmuir-Hinshelwood mechanisms have been proposed. However, to the best of our knowledge, there is no study where the formation of both carbonate and formate is taken into account while deriving the rate expression. The kinetic studies done by Tsipouriari and Verykios over Ni/La_2O_3, CH_4 dissociation and C-gasification via surface carbonates were proposed to be the rate determining step [68]. In the present work, DRIFTS study showed the presence of carbonates and formates on the catalyst surface in addition to adsorbed CH_4, CO_2 and CO. However, no signs of CH_x and CH_xO (formyl) species were observed. TEM studies showed the presence of carbon on the surface of spent catalyst. Hence, the oxidation of the

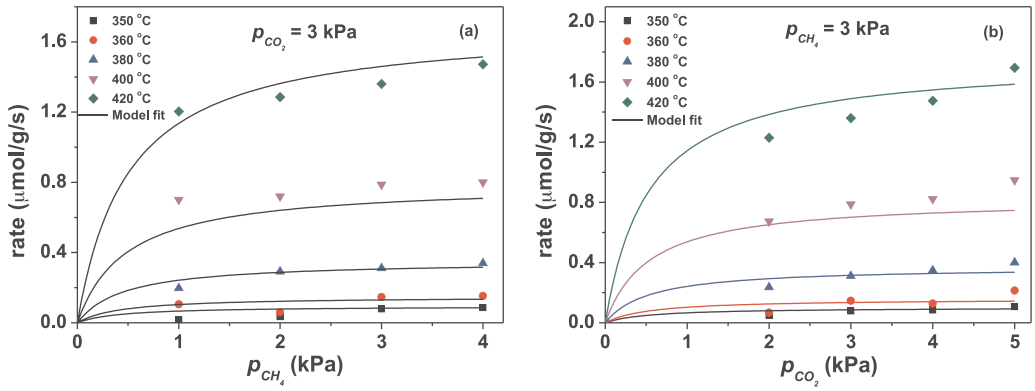

Fig. 17. Variation of rate of CH_4 over $Ce_2Zr_{1.96}Pt_{0.04}O_{7-\delta}$ with (a) partial pressure of CH_4 at constant p_{CO_2} (b) partial pressure of CO_2 at constant p_{CH_4}.

Table 3
Rate parameters obtained after fitting of $Ce_2Zr_{1.96}Pt_{0.04}O_{7-\delta}$.

Parameters	$Ce_2Zr_{1.96}Pt_{0.04}O_{7-\delta}$
k_2	$(2.49 \pm 0.05) \times 10^5 \exp\left(\frac{-17817 \pm 65}{T}\right)$
K_4	$(2.2 \pm 0.6) \exp\left(\frac{-1269 \pm 17}{T}\right)$
K_7	$(8.46 \pm 0.8) \times 10^4 \exp\left(\frac{-16129 \pm 70}{T}\right)$

deposited carbon by lattice oxygen or by carbonates is an important step in the mechanism. High apparent activation energy of CH_4 than CO_2 (see Section 3.4.1), suggests that CH_4 dissociation can be rate determining step over $Ce_2Zr_{1.96}Pt_{0.04}O_{7-\delta}$ [48]. Thus, based on the above discussion, the following mechanism has been proposed on $Ce_2Zr_{1.96}Pt_{0.04}O_{7-\delta}$:

$$CH_4 + Pt \overset{K_1}{\longleftrightarrow} CH_4 - Pt \tag{R-1}$$

$$CH_4 - Pt \overset{k_2}{\longrightarrow} C - Pt + 2H_2 \quad (RDS) \tag{R-2}$$

$$H_2 + 2Pt \overset{K_3}{\longleftrightarrow} 2H - Pt \tag{R-3}$$

$$CO_2 + CZO \overset{K_4}{\longleftrightarrow} CZ - CO_3 \tag{R-4}$$

$$CO_2 + CZ \overset{K_5}{\longleftrightarrow} CO_2 - CZ \tag{R-5}$$

$$CO_2 - CZ \overset{K_6}{\longleftrightarrow} CO + CZO \tag{R-6}$$

$$CO_3 - CZ + C - Pt \overset{k_7}{\longrightarrow} 2CO + Pt + CZO \tag{R-7}$$

$$CO_2 - CZ + H - Pt \overset{K_8}{\longleftrightarrow} HCO_2 - CZ + Pt \tag{R-8}$$

$$HCO_2 - CZ \overset{K_9}{\longleftrightarrow} CO + HO - CZ \tag{R-9}$$

$$C - Pt + CZO \overset{k_{10}}{\longrightarrow} CO - Pt + CZ \tag{R-10}$$

$$CO - Pt \overset{K_{11}}{\longleftrightarrow} CO + Pt \tag{R-11}$$

The comprehensive derivation of mechanism based on above elementary step has been included in Supplementary information. The final rate law over $Ce_2Zr_{1.96}Pt_{0.04}O_{7-\delta}$ was found to be

$$r = \frac{k_2 k_7 K_4 P_{CH_4} P_{CO_2}}{k_7 K_4 P_{CH_4} P_{CO_2} + k_2(1 + K_4 P_{CO_2})} \tag{1}$$

Eq. (1) can be rewritten as

$$\frac{1}{r} = \frac{1}{k_2} + \left(\frac{1 + K_4 P_{CO_2}}{K_4 k_7 P_{CO_2}}\right)\frac{1}{P_{CH_4}} \tag{2}$$

$$\frac{1}{r} = \left(\frac{1}{k_2} + \frac{1}{k_7 P_{CH_4}}\right) + \left(\frac{1}{K_4 k_7 P_{CH_4}}\right)\frac{1}{P_{CO_2}} \tag{3}$$

Eqs. (2) and (3) indicate that the linear dependence between 1/r and $1/P_{CH_4}$ at constant P_{CO_2} and 1/r and $1/P_{CO_2}$ at constant P_{CH_4}. Therefore, the inverse of experimental rate *vs* $1/P_{CH_4}$ at (constant P_{CO_2}) and $1/P_{CO_2}$ (constant P_{CH_4}) were plotted and found to be linear. The regressed values of k_2, K_4 and K_7 were obtained from the slope and intercept of the two linear plots, using the dependence from Eqs. (2) and (3). Then, Eq. (1) was fitted with the experimental data using the values of parameters obtained by the linear regression. Fig. 17 shows the experimental data with the rate Eq. (1). Table 3 enlists the value of rate parameters obtained after fitting.

5. Conclusions

Detailed structural characterization (XRD, XPS, TEM) was performed for the synthesized samples. XRD exhibited the presence of pure pyrochlore phase for NM substituted $Ce_2Zr_2O_7$ pyrochlores. However, Pt substituted $Ce_2Ti_2O_7$ pyrochlores showed the formation of other oxide phases. XPS analysis on $Ce_2Zr_{1.96}Pt_{0.04}O_{7-\delta}$ showed the presence of Ce^{3+} and Ce^{4+} in the XP spectra of Ce 3d, which suggests the formation of $Ce_2Zr_2O_{7+x}$ compound. The appearance of Pt^0 in the XP spectra of Pt 4f recorded after the reaction was due to the presence of reducing atmosphere. TEM exhibited the narrow size distribution of particle size in all the synthesized samples and no significant increase in particle size was observed in the spent catalysts, indicating high thermal stability. Amongst the synthesized materials, $Ce_2Zr_{1.96}Pt_{0.04}O_{7-\delta}$ was found to be highly active for DRM and the time on stream studies demonstrates high stability and coke resistance. Low coke deposition is indicative of the ease of availability of lattice oxygen in $Ce_2Zr_2O_{7+x}$, as observed in H_2 reduction studies. Syngas ratio was enhanced by the addition of O_2 in the feed (ATR) indicating the suppression of RWGS. At higher temperature, DRIFTS studies on $Ce_2Zr_{1.96}Pt_{0.04}O_{7-\delta}$ displayed the development of CO band as a result of decomposition of formates and carbonates, which was true for all the three reforming routes. Based on DRIFTS and kinetic studies, the reaction mechanism was proposed to occur on $Ce_2Zr_{1.96}Pt_{0.04}O_{7-\delta}$ via formate formation indicating the involvement of support during the reaction.

CRediT authorship contribution statement

Disha Jain: Conceptualization, Methodology, Data curation, Visualization, Investigation, Writing - original draft, Writing - review & editing. **Shreya Saha:** Investigation.

Declaration of Competing Interest

The authors declare that they have no known competing financial

interests or personal relationships that could have appeared to influence the work reported in this paper.

Acknowledgements

The authors thank Department of Science and Technology (DST) for financial support. The authors would like to thank Micro and Nano fabrication unit, CeNSE, IISc for XRD and XPS facility, Advanced Facility for Microscopy and Microanalysis, IISc for TEM facility. The authors are grateful to Varadharaja Perumal for his assistance in recording XPS data and Kumari Sushmita for performing TGA. The authors are thankful to Prof. Giridhar Madras for providing research facilities for this work.

Appendix A. Supplementary data

Supplementary material related to this article can be found, in the online version, at doi:https://doi.org/10.1016/j.mcat.2020.110964.

References

[1] M.C. Alvarez-Galvan, N. Mota, M. Ojeda, S. Rojas, R.M. Navarro, J.L.G. Fierro, Direct methane conversion routes to chemicals and fuels, Catal. Today 171 (2011) 15–23.
[2] N. Kumar, M. Shojaee, J.J. Spivey, Catalytic Bi-Reforming of methane: from greenhouse gases to syngas, Curr. Opin. Chem. Eng. 9 (2015) 8–15.
[3] M. Bradford, M. Vannice, CO_2Reforming of CH_4, Catal. Rev. 41 (1999) 1–42.
[4] F. Polo-Garzon, D. Pakhare, J.J. Spivey, D.A. Bruce, Dry reforming of methane on Rh-doped pyrochlore catalysts: a steady-state isotopic transient kinetic study, ACS Catal. 6 (2016) 3826–3833.
[5] S. Zhang, S. Muratsugu, N. Ishiguro, M. Tada, Ceria-doped Ni/SBA-16 catalysts for dry reforming of methane, ACS Catal. 3 (2013) 1855–1864.
[6] M.A. Vasiliades, P. Djinovic, A. Pintar, J. Kovac, A.M. Efstathiou, The effect of CeO_2-ZrO_2 structural differences on the origin and reactivity of carbon formed during methane dry reforming over NiCo/CeO_2-ZrO_2 catalysts studied by transient techniques, Catal. Sci. Technol. 7 (2017) 5422–5434.
[7] D. Pakhare, J. Spivey, A review of dry (CO_2) reforming of methane over noble metal catalysts, Chem. Soc. Rev. 43 (2014) 7813–7837.
[8] D. Pakhare, H. Wu, S. Narendra, V. Abdelsayed, D. Haynes, D. Shekhawat, D. Berry, J. Spivey, Characterization and activity study of the Rh-substituted pyrochlores for CO_2 (dry) reforming of CH_4, Appl. Petrochem. Res. 3 (2013) 117–129.
[9] P. Djinović, J. Batista, A. Pintar, Efficient catalytic abatement of greenhouse gases: methane reforming with CO_2 using a novel and thermally stable Rh–CeO_2 catalyst, Int. J. Hydrogen Energy 37 (2012) 2699–2707.
[10] A.D. Ballarini, S.R. de Miguel, E.L. Jablonski, O.A. Scelza, A.A. Castro, Reforming of CH_4 with CO_2 on Pt-supported catalysts: effect of the support on the catalytic behaviour, Catal. Today 107 (2005) 481–486.
[11] A.K. Avetisov, J.R. Rostrup-Nielsen, V.L. Kuchaev, J.-H. Bak Hansen, A.G. Zyskin, E.N. Shapatina, Steady-state kinetics and mechanism of methane reforming with steam and carbon dioxide over Ni catalyst, J. Mol. Catal. A: Chem. 315 (2010) 155–162.
[12] M.C.J. Bradford, M.A. Vannice, Catalytic reforming of methane with carbon dioxide over nickel catalysts II. Reaction kinetics, Appl. Catal. A 142 (1996) 97–122.
[13] Y.-H. Chin, C. Buda, M. Neurock, E. Iglesia, Consequences of metal–oxide interconversion for C–H bond activation during CH_4 reactions on Pd catalysts, J. Am. Chem. Soc. 135 (2013) 15425–15442.
[14] Y. Wang, R. Zhang, J. Li, L. Li, S. Lin, First-principles study on transition metal-doped anatase TiO_2, Nanoscale Res. Lett. 9 (2014) 46–53.
[15] X. Pan, M.-Q. Yang, X. Fu, N. Zhang, Y.-J. Xu, Defective TiO_2 with oxygen vacancies: synthesis, properties and photocatalytic applications, Nanoscale 5 (2013) 3601–3614.
[16] H. Schwarz, P. González-Navarrete, J. Li, M. Schlangen, X. Sun, T. Weiske, S. Zhou, Unexpected mechanistic variants in the thermal gas-phase activation of methane, Organometallics 36 (2016) 8–17.
[17] H. Schwarz, Doping effects in cluster-mediated bond activation, Angew. Chem. Int. Ed. 54 (2015) 10090–10100.
[18] X. Fang, X. Zhang, Y. Guo, M. Chen, W. Liu, X. Xu, H. Peng, Z. Gao, X. Wang, C. Li, Highly active and stable Ni/$Y_2Zr_2O_7$ catalysts for methane steam reforming: on the nature and effective preparation method of the pyrochlore support, Int. J. Hydrogen Energy 41 (2016) 11141–11153.
[19] D. Pakhare, V. Schwartz, V. Abdelsayed, D. Haynes, D. Shekhawat, J. Poston, J. Spivey, Kinetic and mechanistic study of dry (CO_2) reforming of methane over Rh-substituted $La_2Zr_2O_7$ pyrochlores, J. Catal. 316 (2014) 78–92.
[20] S. Gaur, D.J. Haynes, J.J. Spivey, Rh, Ni, and Ca substituted pyrochlore catalysts for dry reforming of methane, Appl. Catal. A 403 (2011) 142–151.
[21] S. Gaur, D. Pakhare, H. Wu, D.J. Haynes, J.J. Spivey, CO_2 reforming of CH_4 over Ru-substituted pyrochlore catalysts: effects of temperature and reactant feed ratio, Energy Fuels 26 (2012) 1989–1998.
[22] M.A. Vasiliades, P. Djinović, L.F. Davlyatova, A. Pintar, A.M. Efstathiou, Origin and reactivity of active and inactive carbon formed during drm over ni/$ce_{0.38}zr_{0.62}o_{2-\delta}$ studied by transient isotopic techniques, Catal. Today 299 (2018) 201–211.
[23] M.A. Vasiliades, M.M. Makri, P. Djinović, B. Erjavec, A. Pintar, A.M. Efstathiou, Dry reforming of methane over 5 wt% Ni/$Ce_{1-x}Pr_xO_{2-\delta}$ catalysts: performance and characterisation of active and inactive carbon by transient isotopic techniques, Appl. Catal. B 197 (2016) 168–183.
[24] A. Wolfbeisser, O. Sophiphun, J. Bernardi, J. Wittayakun, K. Föttinger, G. Rupprechter, Methane dry reforming over ceria-zirconia supported Ni catalysts, Catal. Today 277 (2016) 234–245.
[25] A. Kambolis, H. Matralis, A. Trovarelli, C. Papadopoulou, Ni/CeO_2-ZrO_2 catalysts for the dry reforming of methane, Appl. Catal. A 377 (2010) 16–26.
[26] M. Tada, S. Zhang, S. Malwadkar, N. Ishiguro, J.-i. Soga, Y. Nagai, K. Tezuka, H. Imoto, S. Otsuka-Yao-Matsuo, S.-i. Ohkoshi, Y. Iwasawa, The active phase of nickel/ordered $Ce_2Zr_2O_X$ catalysts with a discontinuity (x = 7–8) in methane steam reforming, Angew. Chem. 124 (2012) 9495–9499.
[27] S.N. Achary, S.K. Sali, N.K. Kulkarni, P.S.R. Krishna, A.B. Shinde, A.K. Tyagi, Intercalation/deintercalation of oxygen: a sequential evolution of phases in Ce_2O_3/CeO_2 − ZrO_2 pyrochlores, Chem. Mater. 21 (2009) 5848–5859.
[28] H. Kishimoto, T. Omata, S. Otsuka-Yao-Matsuo, K. Ueda, H. Hosono, H. Kawazoe, Crystal structure of metastable κ-$CeZrO_4$ phase possessing an ordered arrangement of Ce and Zr ions, J. Alloys Compd. 312 (2000) 94–103.
[29] T. Sasaki, Y. Ukyo, K. Kuroda, S. Arai, S. Muto, H. Saka, Crystal structure of $Ce_2Zr_2O_7$ and $Ce_2Zr_2O_{7.5}$, J. Ceram. Soc. Jpn. 112 (2004) 440–444.
[30] T. Montini, M.A. Banares, N. Hickey, R. Di Monte, P. Fornasiero, J. Kaspar, M. Graziani, Promotion of reduction in $Ce_{0.5}Zr_{0.5}O_2$: the pyrochlore structure as effect rather than cause? PCCP 6 (2004) 1–3.
[31] S. Arai, S. Muto, T. Sasaki, K. Tatsumi, Y. Ukyo, K. Kuroda, H. Saka, Novel valence state of cerium in $Ce_2Zr_2O_{7.5}$ elucidated by electron energy-loss spectroscopy under electron channeling conditions, Solid State Commun. 135 (2005) 664–667.
[32] P. Burroughs, A. Hamnett, A.F. Orchard, G. Thornton, Satellite structure in the X-ray photoelectron spectra of some binary and mixed oxides of lanthanum and cerium, J. Chem. Soc., Dalton Trans. 0 (1976) 1686–1698.
[33] C. Morant, J.M. Sanz, L. Galan, L. Soriano, F. Rueda, An XPS study of the interaction of oxygen with zirconium, Surf. Sci. 218 (1989) 331–345.
[34] S. Tsunekawa, K. Asami, S. Ito, M. Yashima, T. Sugimoto, XPS study of the phase transition in pure zirconium oxide nanocrystallites, Appl. Surf. Sci. 252 (2005) 1651–1656.
[35] M. Romeo, K. Bak, J. El Fallah, F. Le Normand, L. Hilaire, XPS study of the reduction of cerium dioxide, Surf. Interface Anal. 20 (1993) 508–512.
[36] M.C. Biesinger, L.W.M. Lau, A.R. Gerson, R.S.C. Smart, Resolving surface chemical states in XPS analysis of first row transition metals, oxides and hydroxides: Sc, Ti, V, Cu and Zn, Appl. Surf. Sci. 257 (2010) 887–898.
[37] B. Richter, H. Kuhlenbeck, H.-J. Freund, P.S. Bagus, Cluster core-level binding-energy shifts: the role of lattice strain, Phys. Rev. Lett. 93 (2004) 026805–026808.
[38] R. Nyholm, N. Martensson, A. Lebugle, U. Axelsson, Auger and Coster-Kronig broadening effects in the 2p and 3p photoelectron spectra from the metals ^{22}Ti-^{30}Zn, J. Phys. F: Met. Phys. 11 (1981) 1727–1733.
[39] C.C. Wang, S.S. Siao, J.C. Jiang, C–H bond activation of methane via σ–δ interaction on the IrO_2 (110) surface: density functional theory study, J. Phys. Chem. C 116 (2012) 6367–6370.
[40] D. Jain, G. Madras, Mechanistic insights and kinetics of CO oxidation over pristine and noble metal modified Fe_2O_3 using DRIFTS, Ind. Eng. Chem. Res. 56 (2017) 2008–2024.
[41] D.J. Morgan, Resolving ruthenium: XPS studies of common ruthenium materials, Surf. Interface Anal. 47 (2015) 1072–1079.
[42] T. Baidya, M.S. Hegde, J. Gopalakrishnan, Oxygen-release/storage properties of $Ce_{0.5}M_{0.5}O_2$ (M = Zr, Hf) oxides: interplay of crystal chemistry and electronic structure, J. Phys. Chem. B 111 (2007) 5149–5154.
[43] D.J. Haynes, A. Campos, D.A. Berry, D. Shekhawat, A. Roy, J.J. Spivey, Catalytic partial oxidation of a diesel surrogate fuel using an Ru-substituted pyrochlore, Catal. Today 155 (2010) 84–91.
[44] G. Avgouropoulos, T. Ioannides, TPD and TPSR study of CO interaction with CuO–CeO_2 catalysts, J. Mol. Catal. A: Chem. 296 (2008) 47–53.
[45] M. Fadoni, L. Lucarelli, Temperature programmed desorption, reduction, oxidation and flow chemisorption for the characterisation of heterogeneous catalysts. Theoretical aspects, instrumentation and applications, in: A. Dąbrowski (Ed.), Temperature Programmed Desorption, Reduction, Oxidation and Flow Chemisorption for the Characterisation of Heterogeneous Catalysts. Theoretical Aspects, Instrumentation and Applications, Elsevier, Amsterdam, 1999, pp. 177–225.
[46] J.A. Kilner, Fast oxygen transport in acceptor doped oxides, Solid State Ion. 129 (2000) 13–23.
[47] V. Butler, C.R.A. Catlow, B.E.F. Fender, J.H. Harding, Dopant ion radius and ionic conductivity in cerium dioxide, Solid State Ion. 8 (1983) 109–113.
[48] D. Pakhare, C. Shaw, D. Haynes, D. Shekhawat, J. Spivey, Effect of reaction temperature on activity of Pt- and Ru-substituted lanthanum zirconate pyrochlores ($La_2Zr_2O_7$) for dry (CO_2) reforming of methane (DRM), J. CO2 Util. 1 (2013) 37–42.
[49] J. Wei, E. Iglesia, Structural requirements and reaction pathways in methane activation and chemical conversion catalyzed by rhodium, J. Catal. 225 (2004) 116–127.
[50] G. Sierra Gallego, C. Batiot-Dupeyrat, J. Barrault, F. Mondragón, Dual active-site mechanism for dry methane reforming over Ni/La_2O_3 produced from $LaNiO_3$ perovskite, Ind. Eng. Chem. Res. 47 (2008) 9272–9278.
[51] R.C. Rabelo-Neto, H.B.E. Sales, C.V.M. Inocêncio, E. Varga, A. Oszko, A. Erdohelyi, F.B. Noronha, L.V. Mattos, CO_2 reforming of methane over supported $LaNiO_3$ perovskite-type oxides, Appl. Catal. B 221 (2018) 349–361.

[52] W. Wang, S.M. Stagg-Williams, F.B. Noronha, L.V. Mattos, F.B. Passos, Partial oxidation and combined reforming of methane on Ce-promoted catalysts, Catal. Today 98 (2004) 553–563.
[53] M.P. Kohn, M.J. Castaldi, R.J. Farrauto, Auto-thermal and dry reforming of landfill gas over a Rh/γAl_2O_3 monolith catalyst, Appl. Catal. B 94 (2010) 125–133.
[54] C. Li, G. Li, Q. Xin, FT-IR spectroscopic studies of methane adsorption on magnesium oxide, J. Phys. Chem. A 98 (1994) 1933–1938.
[55] P. Bazin, O. Saur, J. Lavalley, M. Daturi, G. Blanchard, FT-IR study of CO adsorption on Pt/CeO_2: characterisation and structural rearrangement of small Pt particles, PCCP 7 (2005) 187–194.
[56] C. Li, Q. Xin, FT-IR spectroscopic investigation of methane adsorption on cerium oxide, J. Phys. Chem. A 96 (1992) 7714–7718.
[57] J.F. Múnera, S. Irusta, L.M. Cornaglia, E.A. Lombardo, D.V. Cesar, M. Schmal, Kinetics and reaction pathway of the CO_2 reforming of methane on Rh supported on lanthanum-based solid, J. Catal. 245 (2007) 25–34.
[58] M. Tsiouris, M.D. Wheeler, M.I. Lester, Activation of the CH stretching vibrations in CH_4-OH entrance channel complexes: spectroscopy and dynamics, J. Chem. Phys. 114 (2001) 187–197.
[59] P.G. Lustemberg, M.V. Bosco, A. Bonivardi, H.F. Busnengo, M.V. Ganduglia-Pirovano, Insights into the nature of formate species in the decomposition and reaction of methanol over cerium oxide surfaces: a combined infrared spectroscopy and density functional theory study, J. Phys. Chem. C 119 (2015) 21452–21464.
[60] D. Heyl, U. Rodemerck, U. Bentrup, Mechanistic study of low-temperature CO_2 hydrogenation over modified Rh/Al_2O_3 catalysts, ACS Catal. 6 (2016) 6275–6284.
[61] T. Chafikab, S. Kameokab, Y. Ukisub, T. Miyaderab, *In situ* diffuse reflectance infrared fourier transform spectroscopy study of surface species involved in NO_x reduction by ethanol over alumina-supported silver catalyst, J. Mol. Catal. A: Chem. 136 (1998) 203–211.
[62] Z. Zhang, X.E. Verykios, S.M. MacDonald, S. Affrossman, Comparative study of carbon dioxide reforming of methane to synthesis gas over Ni/La_2O_3 and conventional nickel-based catalysts, J. Phys. Chem. A 100 (1996) 744–754.
[63] J.T. Richardson, S.A. Paripatyadar, Carbon dioxide reforming of methane with supported rhodium, Appl. Catal. 61 (1990) 293–309.
[64] N. Laosiripojana, W. Sutthisripok, S. Assabumrungrat, Synthesis gas production from dry reforming of methane over CeO_2 doped Ni/Al_2O_3: influence of the doping ceria on the resistance toward carbon formation, Chem. Eng. J. 112 (2005) 13–22.
[65] F. Wang, L. Xu, J. Zhang, Y. Zhao, H. Li, H.X. Li, K. Wu, G.Q. Xu, W. Chen, Tuning the metal-support interaction in catalysts for highly efficient methane dry reforming reaction, Appl. Catal. B 180 (2016) 511–520.
[66] Z.L. Zhang, X.E. Verykios, Carbon dioxide reforming of methane to synthesis gas over supported Ni catalysts, Catal. Today 21 (1994) 589–595.
[67] M.M. Barroso Quiroga, A.E. Castro Luna, Kinetic analysis of rate data for dry reforming of methane, Ind. Eng. Chem. Res. 46 (2007) 5265–5270.
[68] V.A. Tsipouriari, X.E. Verykios, Kinetic study of the catalytic reforming of methane with carbon dioxide to synthesis gas over Ni/La_2O_3 catalyst, Catal. Today 64 (2001) 83–90.
[69] C. Pichas, P. Pomonis, D. Petrakis, A. Ladavos, Kinetic study of the catalytic dry reforming of CH_4 with CO_2 over $La_{2-x}Sr_xNiO_4$ perovskite-type oxides, Appl. Catal. A 386 (2010) 116–123.